

Pressure- and Rate-Transient Model for an Array of Interfering Fractured Horizontal Wells in Unconventional Reservoirs

Erdal Ozkan^{1*}  and Meruyert Makhatova¹ 

¹Colorado School of Mines

Summary

An analytical solution is presented for pressure- and rate-transient behavior of an array of n parallel and fractured horizontal wells in an unconventional reservoir. Wells are of equal length but otherwise of unidentical properties. Each well has an arbitrary number of uniformly spaced identical, finite-conductivity fractures and is surrounded by a stimulated reservoir volume (SRV). The properties of hydraulic fractures (HFs) and SRVs may vary from well to well. Different properties may also be assigned to the unstimulated reservoir sections between wells. Natural fractures in stimulated and unstimulated reservoir volumes are accounted for by transient dual-porosity idealization. The flow domain is divided into blocks of 1D flow under the trilinear-flow assumption. Solution for each block is obtained analytically and coupled with the solutions for the neighboring blocks by the continuity of pressure and flux at the block interfaces. Drainage volumes of wells are adjusted based on the variation of well production rates because of moving no-flow boundaries between wells. The superposition principle is applied to consider variable-production conditions as well as nonsynchronous production and shut-in schedules of wells. The final solution is in the form of a matrix-vector equation in the Laplace transform domain and inverted into the time domain numerically. The model is robust and reasonably accurate for most practical applications of single-phase oil and gas production from multiple wells in an unconventional reservoir. It is an efficient tool to assess well interference effects for different well completion designs and varying reservoir characteristics. The speed of the model makes it useful for pressure-transient and production-data analysis, as well as for the initial calibration and verification of more complex numerical models.

Introduction

Interest in the interference of horizontal wells in multiwell pads has increased as the development plans required smaller well spacings in unconventional reservoirs (e.g., Ajani and Kelkar 2012; Kurtoglu and Salman 2015; Molina 2019; Chu et al. 2019, 2020a, 2020b; Hamdi et al. 2021; Lerza et al. 2022; Acuna 2023). Although infill drilling is expected to increase productivity by smaller per-well drainage areas, in some cases, drilling and stimulation of infill (child) wells may damage the productivity of existing (parent) wells due to so-called “frac-hits.” In these cases, concerns arise from the perspective of optimizing the perils of frac-hits with the benefits of smaller well drainage areas. Addressing such concerns requires considering multiple productivity realizations under different well-spacing and completion scenarios. Numerical models of multiwell systems entangled with complex unconventional-reservoir characteristics are usually too elaborate for sensitivity studies and analytical (or semi-analytical) models may better serve the purpose.

Several analytical models have been presented in the literature using different simplifications of the multiwell interference problem for analytical treatment (e.g., Molina 2019; Chu et al. 2020b; Hamdi et al. 2021). Their validity depends on the success of the underlying assumptions in approximating physical reality. The objective of this work is to develop a robust, practical, analytical solution for interfering horizontal wells in a single-layer, unconventional reservoir. The model is intended for the pressure-transient and production behavior of wells under the trilinear-flow assumption (Brown et al. 2011). Differences between our model and those in the literature are expressed in the “Discussion” section below.

We consider a closed reservoir sector containing n parallel and hydraulically fractured horizontal wells of equal length in a single file. The sector is divided into blocks of SRVs surrounding each well and unstimulated, outer reservoir volumes (ORVs) between wells. Blocks may have different properties including dual porosity. HFs are also represented by thin rectangular blocks. HF conductivities, half-lengths, and spacings are uniform on each well but may vary from well to well. Solutions for reservoir blocks are obtained analytically by considering the continuity of pressure and flux at block interfaces to account for the interference of neighboring blocks and wells. This approach leads to a nested analytical solution in the Laplace domain, which is inverted to the time domain numerically.

To obtain a reasonably accurate yet practical and computationally convenient solution, some assumptions are made in the representation of the physical system. The stimulation effect due to hydraulic fracturing is represented by a denser, better connected, and more pervasive network of higher conductivity fractures in the reservoir. Changing the properties of reservoir fractures and the sizes of matrix blocks enables considering different levels of stimulation effectiveness. Fractured reservoirs are represented by transient dual-porosity idealization (Kazemi 1969; de Swaan 1976). The flow in each reservoir block is assumed to be 1D and the blocks of ORV, SRV, and HF are connected under the trilinear-flow idealization (Brown et al. 2011). The speed and convenience of numerical evaluations of the proposed solution surpass those of other analytical and numerical approaches, and the level of numerical accuracy meets the requirements for pressure- and rate-transient analyses (PTA and RTA, respectively) applications within the bounds of the modeling assumptions.

No claim is made on the inclusiveness of the model for a broad range of physical conditions encountered in the field. Statements on numerical precision are of an algorithmic nature. As a broad disclaimer, the multiwell interference model presented here should be applicable where trilinear flow is a reasonable assumption for each well. The model is a forward solution for performance predictions, well completion and stimulation design, well-spacing considerations, and a first approximation to well-interference predictions. For the PTA and RTA applications, production-data analysis, and prediction of stimulation effectiveness, it must be incorporated into an inverse

*Corresponding author; email: eozkan@mines.edu

Copyright © 2024 Society of Petroleum Engineers

This paper (SPE 215031) was accepted for presentation at the SPE Annual Technical Conference and Exhibition, San Antonio, Texas, USA, 16–18 October 2023, and revised for publication. Original manuscript received for review 19 October 2023. Revised manuscript received for review 22 April 2024. Paper peer approved 25 April 2024.

solution algorithm (matching observed responses with assumed model input) and a diagnostic identification procedure (identification of expected flow regime characteristics) must be implemented.

Below, we first describe our conceptual construction of the multiwell model, state the assumptions, and define the dimensionless variables and notations used in the solution. Then, we present the algorithm for the analytical solution. Some details of the derivations are given in the appendices. Verification of the solution and discussions of synthetic and field examples demonstrate the utility of the model. A brief discussion to highlight the differences of our model from those in the literature is also presented.

Model and Definitions

Here, we explain the construction of the conceptual model and provide the definitions of dimensionless variables.

Conceptual Model. Fig. 1 shows an array of three fractured horizontal wells in a single file. However, the solution is general for n wells. Wells are of equal length and possess an arbitrary number of uniformly spaced, identical, finite-conductivity HFs. The spacing of HF treatments (number of HFs) as well as the half-lengths and conductivities of HFs may change from well to well. Each well has an SRV enclosing the well and its HFs. The stimulation effect is envisioned as a pervasive network of reservoir fractures in the SRV between HFs, which may include pre-existing (active and rejuvenated) and induced fractures. For notational convenience, fractures in the SRV are called natural fractures. Matrix and natural fractures in the SRVs are deemed overlapping continua and modeled by the transient, dual-porosity idealization (Kazemi 1969; de Swaan 1976). Unstimulated reservoir sections between SRVs are denoted as ORVs. ORVs may be the original (virgin) reservoir sections, with or without natural fractures, or may have varying degrees of stimulation effect from the treatments of the neighboring wells. Each SRV and ORV has its own dual-porosity reservoir characteristics.

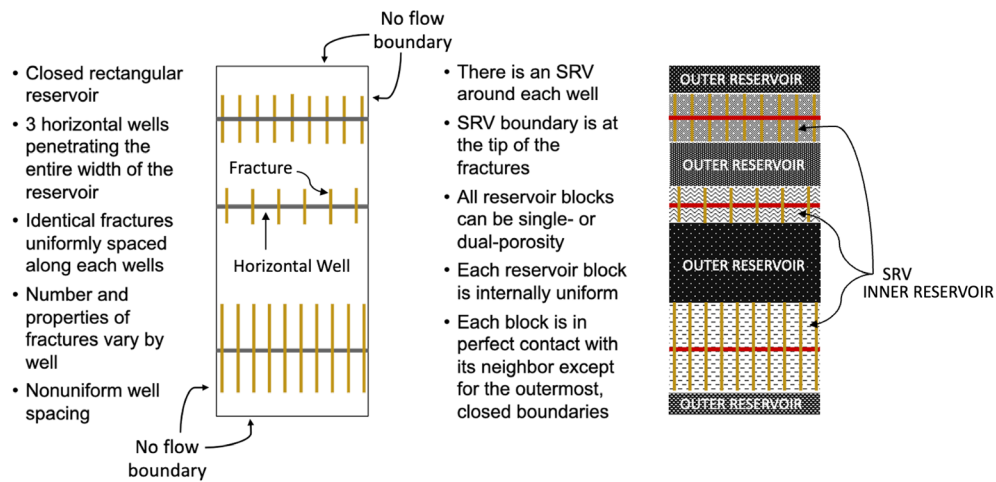


Fig. 1—Sketch of an array of three fractured horizontal wells.

The array of wells is enclosed in a closed, rectangular reservoir sector (Fig. 1). The no-flow boundaries of the sector are assumed to be formed by the neighboring arrays of wells or by physical conditions. The sector boundaries normal to the well axes are located at the well tips; that is, the width of the sector is equal to the length of the horizontal wells (assumed to be identical). The length of the sector depends on the number of wells and assumed SRV widths (fracture half-lengths) and ORV widths (spacings between SRVs). The locations of the boundaries between wells (parallel to the well axes) are not predetermined; they form and move depending on the changing interference between wells because of varying flow conditions.

In our notation, the block including Well i and its SRV is called the inner reservoir and denoted by I_i . Unstimulated reservoir blocks (ORVs) between inner reservoir blocks are called the outer reservoir and denoted by O_i . With this notation, we have n inner reservoirs and $n + 1$ outer reservoirs (Fig. 2). Subscript F is used to denote properties belonging to the HFs of a well (assumed identical for each well), and subscripts f and m denote natural fracture and matrix properties, respectively.

Trilinear-flow assumption (Brown et al. 2011) and uniformly distributed, identical fractures along each well allow us to use a repetitive (symmetry) element in the derivations (Fig. 3). Flow in each reservoir block is solved subject to the continuity of pressure and flux at the boundary with the neighboring blocks (Fig. 4). Pressure interference from neighboring wells enters the solution of each well through its SRV boundary conditions. In the trilinear-flow model, flow in the SRV is 1D and parallel to the well (parallel to the SRV boundary and perpendicular to HF planes). Although the pressure changes along the SRV boundary, flow in the ORV is assumed to be pseudo-1D and normal to the SRV boundary. This physically implies that the ORVs act as pressure-averaging media in a direction parallel to the SRV boundaries. Accordingly, the interference of neighboring wells enters the solution of a given well in terms of the average pressures of the neighboring wells along their SRV boundaries.

Definitions. We express the solution in terms of dimensionless variables and use the definitions of transient, dual-porosity model parameters.

Dimensionless Variables. To define common dimensionless variables for all reservoir blocks, we use reference properties denoted by the subscript R . The reference properties are arbitrary constants, but they possess the units of the corresponding physical properties.

The dimensionless pressure is defined by

$$p_{\ell KiD} = \frac{\psi_1 k_R h}{q_R B \mu} \Delta p_{\ell Ki} = \frac{\psi_1 k_R h}{q_R B \mu} (p_{ini} - p_{\ell Ki}), \quad K = I \text{ or } F \text{ and } i = 1, \dots, n \text{ or } K = O \text{ and } i = 1, \dots, n + 1, \quad (1)$$

O: Outer Reservoir I: Inner Reservoir

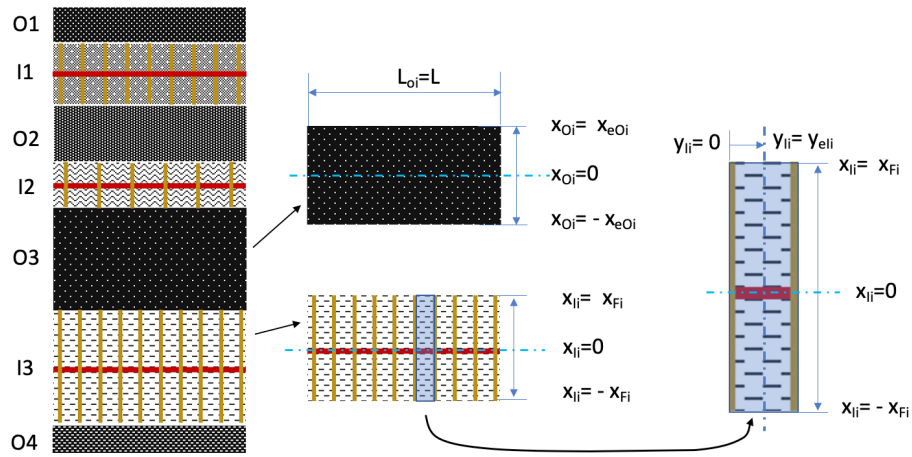


Fig. 2—Decoupling of the three-well array into individual reservoir sections with and without sources (wells).

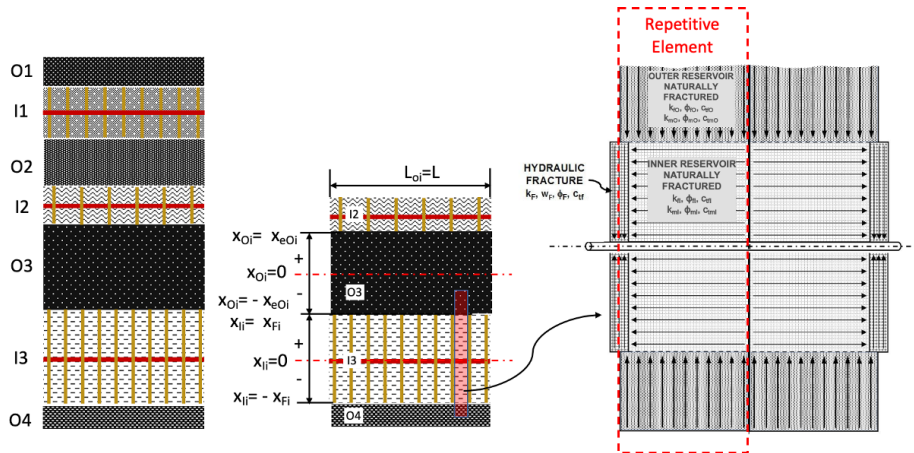


Fig. 3—Trilinear-flow idealization (right) and the repetitive (symmetry) element between two HF along a well.

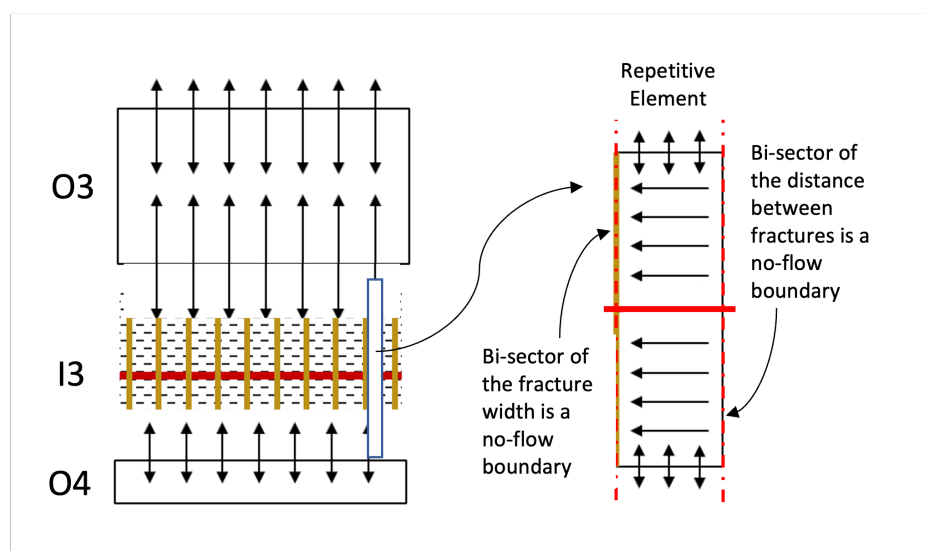


Fig. 4—Coupling of flows at segment boundaries in source (well) solutions.

where p_{ini} is the initial pressure of the reservoir and $\ell = m$ for matrix and f for natural fractures. In Eq. 1, ψ_1 is a conversion factor given by

$$\psi_1 = \begin{cases} 2\pi & \text{Consistent Units} \\ 1/141.2 & \text{Field Units.} \end{cases} \quad (2)$$

The definition of dimensionless time is given by

$$t_D = \frac{\eta_R}{x_{FR}^2} t, \quad (3)$$

where η_R is a reference diffusivity defined by

$$\eta_R = \frac{\psi_2 k_R}{(\phi_R c_{tR})_{f+m} \mu}, \quad (4)$$

and x_{FR} is a reference fracture half-length. In Eq. 4, $(\phi_R c_{tR})_{f+m}$ is a reference total-system ($f+m$) storativity, defined by

$$(\phi_R c_{tR})_{f+m} = \phi_R c_{tfR} + \phi_m R c_{tmR}, \quad (5)$$

and ψ_2 is the unit-conversion factor given by

$$\psi_2 = \begin{cases} 1 & \text{Consistent Units} \\ 6.328 \times 10^{-3} & \text{Field Units (} t \text{ in days).} \end{cases} \quad (6)$$

We denote the flow rate of Well i by q_i and the flow rate of each fracture on Well i by q_{Fi} . Also defining a reference (constant) rate by q_R , the dimensionless flow rate of Well i is given by

$$q_{iD} = \frac{q_i}{q_R}; \quad i = 1, \dots, n, \quad (7)$$

where the well rate, q_i , and the HF rate, q_{Fi} , are related by

$$q_i = q_{Fi} n_{Fi}; \quad i = 1, \dots, n. \quad (8)$$

We also define the diffusivities of the inner and outer reservoirs by

$$\eta_{Ki} = \frac{\psi_2 k_{Ki}}{(\phi_{Ki} c_{tKi})_{f+m} \mu}, \quad K = I \text{ and } i = 1, \dots, n \text{ or } K = O \text{ and } i = 1, \dots, n+1, \quad (9)$$

where $(\phi_{Ki} c_{tKi})_{f+m}$ is given by

$$(\phi_{Ki} c_{tKi})_{f+m} = \phi_{Ki} c_{tfKi} + \phi_{mKi} c_{tmKi}; \quad i = 1, \dots, n, \quad (10)$$

and the diffusivities of the HFs are defined by

$$\eta_{Fi} = \frac{\psi_2 k_{Fi}}{\phi_{Fi} c_{tFi} \mu}; \quad i = 1, \dots, n. \quad (11)$$

The following diffusivity ratios are also used:

$$\eta_{KiD} = \frac{\eta_{Ki}}{\eta_R}; \quad i = 1, \dots, n \text{ for } K = I \text{ and HF, or } i = 1, \dots, n+1 \text{ for } K = O, \quad (12)$$

and

$$\eta_{FiD} = \frac{\eta_{Fi}}{\eta_R}; \quad i = 1, \dots, n. \quad (13)$$

The dimensionless distances and lengths in the x -, y -, and z -directions are defined by

$$x_{KiD} = \frac{x_{Ki}}{x_{FR}}; \quad K = I \text{ or HF and } i = 1, \dots, n \text{ or } K = O \text{ and } i = 1, \dots, n+1, \quad (14)$$

$$x_{FiD} = \frac{x_{Fi}}{x_{FR}}; \quad i = 1, \dots, n, \quad (15)$$

$$y_{KiD} = \frac{y_{Ki}}{y_{eli}}; \quad K = I \text{ and } i = 1, \dots, n, \text{ or } K = O \text{ and } i = 1, \dots, n+1, \quad (16)$$

$$\tilde{y}_{eKiD} = \frac{y_{eKi}}{x_{FR}}; \quad K = I \text{ and } i = 1, \dots, n, \text{ or } K = O \text{ and } i = 1, \dots, n + 1, \quad (17)$$

$$w_{FiD} = \frac{w_{Fi}}{x_{FR}}; \quad i = 1, \dots, n, \quad (18)$$

and

$$z_{KiD} = \frac{z_{Ki}}{h_{mKi}/2}; \quad K = I \text{ and } i = 1, \dots, n \text{ or } K = O \text{ and } i = 1, \dots, n + 1. \quad (19)$$

We define the dimensionless formation thickness and dimensionless wellbore radii, respectively, by

$$h_D = \frac{h}{x_{FR}}, \quad (20)$$

and

$$r_{wDi} = \frac{r_{wi}}{x_{FR}}. \quad (21)$$

The dimensionless fracture conductivities are defined by

$$C_{FiD} = \frac{k_{Fi} w_{Fi}}{k_{Jli} x_{Fi}}; \quad i = 1, \dots, n, \quad (22)$$

and the conductivity ratios between the inner reservoir i (Ii) and the outer reservoir j (Oj) are defined by

$$C_{RijD} = \frac{k_{Jli} x_{Fi}}{k_{Oj} y_{eli}}; \quad i = 1, \dots, n \text{ and } j = 1, \dots, n + 1. \quad (23)$$

Finally, we define the dimensionless wellbore storage coefficient by

$$C_{iD} = \frac{\psi_3 C_i}{2\pi (\phi_{Ri} c_{tR})_{f+m} h r_w^2}, \quad (24)$$

where C_i is the wellbore storage coefficient of Well i , and ψ_3 is the unit-conversion coefficient defined by

$$\psi_3 = \begin{cases} 1 & \text{Consistent Units} \\ 5.615 & \text{Field Units.} \end{cases} \quad (25)$$

Dual-Porosity Model and Parameters. We use the transient dual-porosity idealization of Kazemi (1969) and de Swaan (1976) with a stack of alternating, horizontal slabs of matrix and fracture media. The thicknesses of individual matrix and fracture slabs in Reservoir Block Ki ($K = I$ or O) are uniform and denoted, respectively, by h_{mKi} and h_{fKi} . We let n_{mKi} and n_{fKi} denote, respectively, the number of matrix and fracture slabs ($n_{mKi} = n_{fKi}$) and define the total thicknesses of the matrix and fracture slabs, respectively, by $h_{mtKi} = n_{mKi} h_{mKi}$ and $h_{ftKi} = n_{fKi} h_{fKi}$. The solution derived here, however, can be readily extended to other geometries of matrix blocks by replacing the shape and transfer functions defined below by their counterparts for the selected matrix geometry.

We use the bulk definition of the fracture and matrix properties (i.e., the intrinsic property of the medium scaled by the ratio of the medium volume to the total-system volume). The dual-porosity parameters, storativity ratio, ω_{Ki} , and the transmissivity ratio, λ_{Ki} , are defined, respectively, by

$$\omega_{Ki} = \frac{\phi_{fKi} c_{tfKi}}{(\phi_{Ki} c_{tKi})_{f+m}}, \quad K = I \text{ and } i = 1, \dots, n \text{ or } K = O \text{ and } i = 1, \dots, n + 1, \quad (26)$$

and

$$\lambda_{Ki} = \sigma_{Ki} \left(\frac{k_{mKi}}{k_{fKi}} \right) x_{FR}^2, \quad K = I \text{ and } i = 1, \dots, n \text{ or } K = O \text{ and } i = 1, \dots, n + 1. \quad (27)$$

In Eq. 27, $(\phi_{Ki} c_{tKi})_{f+m}$ is the total storativity of Reservoir Block Ki ; that is,

$$(\phi_{Ki} c_{tKi})_{f+m} = \phi_{fKi} c_{tfKi} + \phi_{mKi} c_{tmKi}, \quad K = I \text{ and } i = 1, \dots, n \text{ or } K = O \text{ and } i = 1, \dots, n + 1, \quad (28)$$

and, in Eq. 28, σ_{Ki} is a shape factor for slab matrices given by

$$\sigma_{Ki} = \frac{12}{h_{mKi}^2}, \quad K = I \text{ and } i = 1, \dots, n \text{ or } K = O \text{ and } i = 1, \dots, n + 1. \quad (29)$$

For the transient, dual-porosity, slab-matrix model, the transfer function between matrix and fracture slabs is defined by

$$f_{Ki}(s_{Ki}) = \omega_{Ki} + \sqrt{\frac{\lambda_{Ki}(1-\omega_{Ki})}{3s_{Ki}}} \tanh\left(\sqrt{\frac{3(1-\omega_{Ki})s_{Ki}}{\lambda_{Ki}}}\right), \quad K = I \text{ and } i = 1, \dots, n \text{ or } K = O \text{ and } i = 1, \dots, n+1, \quad (30)$$

where s_{Ki} is the Laplace transform parameter with respect to dimensionless time t_{KiD} given (for Reservoir Block Ki) by

$$t_{KiD} = \frac{\eta_{Ki}}{x_{FR}^2} t, \quad K = I \text{ or HF and } i = 1, \dots, n \text{ or } K = O \text{ and } i = 1, \dots, n+1. \quad (31)$$

The Laplace transform parameter s_{Ki} with respect to t_{KiD} in Eq. 31 is related to the Laplace transform parameter s with respect to the common dimensionless time t_D (Eq. 3) by

$$s_{Ki} = \frac{s}{\eta_{KiD}}, \quad K = I \text{ or HF and } i = 1, \dots, n \text{ or } K = O \text{ and } i = 1, \dots, n+1. \quad (32)$$

For convenience, we also define

$$u_{Ki} = s_{Ki} f_{Ki}(s_{Ki}), \quad K = I \text{ and } i = 1, \dots, n \text{ or } K = O \text{ and } i = 1, \dots, n+1. \quad (33)$$

Definitions of σ_{Ki} , λ_{Ki} , and $f_{Ki}(s_{Ki})$ need to be modified if other matrix geometries and characteristic lengths are used.

Solution for the Multiwell Interference Problem

The inspiring approach for this work is the boundary-element method described by Medeiros et al. (2010). The boundary-element method discretizes the boundary data, but it solves the flow problem within the domain analytically. For the problem considered in this work, we circumvent boundary partitioning by invoking the trilinear-flow idealization proposed by Brown et al. (2011). The trilinear-flow assumption idealizes flow in each block of HF, SRV, and ORV as 1D and mutually perpendicular to each other (**Fig. 3**). When coupling flows between neighboring blocks, averages of pressures and fluxes along their boundaries are considered. This pseudo-1D assumption allows using one boundary node for each boundary. Therefore, the solution approach used in this paper is the same as obtaining 1D analytical solutions for each SRV, ORV, and HF and coupling them with the solution of the neighboring blocks by the continuity of pressure and flux at the boundaries. If capturing the effect of multidimensional pressure variations in each block is desired, then the full boundary-element method must be used with appropriate discretization of the boundaries. This, however, detracts from the convenience and simplicity of the model, and, for most intended applications of this solution, we have found this elaboration excessive for the added accuracy.

Under the general lines described above, the solution of the multiwell interference problem is derived in Appendix A. Here, we present the final form of the solution. The bar signs over the variables (—) in the following presentation indicate the Laplace transform with respect to dimensionless time t_D .

General Solution. The dimensionless pressure solution for Well i is obtained in Appendix A and given (in Laplace domain, by

$$\bar{p}_{wiD} = \frac{\gamma_{Fi}}{\alpha_{Fi}\alpha_{Oi}} \bar{h}_i + r_i; \quad 1 \leq i \leq n, \quad (34)$$

where \bar{h}_i is given by

$$\bar{h}_i = \begin{cases} (\gamma_{O10} + \gamma_{O12}) \bar{p}_{j2D,\text{avg}} & i = 1 \\ \gamma_{Oii-1} \bar{p}_{jIi-1D,\text{avg}} + \gamma_{Oii+1} \bar{p}_{jIi+1D,\text{avg}} & 2 \leq i \leq n-1, \\ (\gamma_{Onn-1} + \gamma_{Onn+1}) \bar{p}_{jIn-1D,\text{avg}} & i = n \end{cases} \quad (35)$$

and

$$r_i = \frac{\pi \bar{q}_{iD}}{n_{Fi} C_{FiD} k_{jIiD} x_{FiD} \sqrt{\alpha_{Fi}} \tanh(\sqrt{\alpha_{Fi}} x_{FiD})}. \quad (36)$$

In Eqs. 34 through 36,

$$\gamma_{Fi} = \frac{2\beta_{Fi}}{C_{FiD} \tilde{y}_{eIiD} x_{FiD}}, \quad (37)$$

$$\alpha_{Fi} = \frac{2\beta_{Fi}}{C_{FiD} \tilde{y}_{eIiD} x_{FiD}} + \frac{s}{\eta_{FiD}}, \quad (38)$$

$$\beta_{Fi} = \sqrt{\alpha_{Oi}} \tanh(\sqrt{\alpha_{Oi}}), \quad (39)$$

$$\gamma_{Oij} = \frac{\sqrt{u_{Oj}} \tilde{y}_{eIiD}}{2C_{RijD} \sinh[2\sqrt{u_{Oj}} x_{eOjD}]}; \quad 1 \leq i, j \leq n, \quad (40)$$

and

$$\alpha_{Oi} = \beta_{Oii} + \beta_{Oii+1} + \tilde{y}_{eIiD}^2 u_{Ii}; \quad i = 1, n. \quad (41)$$

Eq. 34 provides n equations in $2n$ unknowns (n unknowns in \bar{p}_{wiD} and n unknowns in $\bar{p}_{jIiD,\text{avg}}$). We can obtain n additional equations for $\bar{p}_{jIjD,\text{avg}}$ as follows (Appendix B):

$$\bar{p}_{\eta j D, \text{avg}} = \begin{cases} \tau_{11} \bar{p}_{FI1D} + \tau_{12} \bar{p}_{FI2D, \text{avg}} & j = 1 \\ \tau_{jj} \bar{p}_{FIjD} + \tau_{jj-1} \bar{p}_{\eta j-1D, \text{avg}} + \tau_{jj+1} \bar{p}_{\eta j+1D, \text{avg}} & 2 \leq j \leq n-1 \\ \tau_{nn} \bar{p}_{FIuD} + \tau_{nn-1} \bar{p}_{\eta i-1D, \text{avg}} & j = n, \end{cases} \quad (42)$$

where

$$\tau_{ij} = \begin{cases} \varepsilon_i & j = i, \quad 1 \leq i \leq n \\ (1 - \varepsilon_1) \frac{\gamma_{O12}}{\alpha_{O1}} & j = 2, \quad i = 1 \\ (1 - \varepsilon_n) \frac{\gamma_{Onn-1}}{\alpha_{On}} & j = n-1, \quad i = n \\ (1 - \varepsilon_i) \frac{\gamma_{Oij}}{\alpha_{Oi}} & \text{otherwise} \end{cases} \quad (43)$$

and

$$\varepsilon_i = \frac{\tanh(\sqrt{\alpha_{Oi}})}{\sqrt{\alpha_{Oi}}}; \quad i = 1, n. \quad (44)$$

Eqs. 34 and 42 can be rewritten as

$$\sum_{j=1}^{2n} a_{ij} p_j = b_i; \quad 1 \leq i \leq 2n, \quad (45)$$

where

$$p_j = \begin{cases} \bar{p}_{FIjD} & 1 \leq j \leq n \\ \bar{p}_{\eta j-nD, \text{avg}} & n+1 \leq j \leq 2n, \end{cases} \quad (46)$$

$$a_{ij} = \begin{cases} 1 & j = i \quad 1 \leq i \leq n \\ -\frac{\gamma_{Fi}}{\alpha_{Fi}\alpha_{Oi}} (\gamma_{Oii-1} + \gamma_{Oii+1}) & j = i+1+n \quad i = 1 \\ -\frac{\gamma_{Fi}}{\alpha_{Fi}\alpha_{Oi}} \gamma_{Oii-1} & j = i-1+n \quad 2 \leq i \leq n-1 \\ -\frac{\gamma_{Fi}}{\alpha_{Fi}\alpha_{Oi}} \gamma_{Oii+1} & j = i+1+n \quad 2 \leq i \leq n-1 \\ -\frac{\gamma_{Fi}}{\alpha_{Fi}\alpha_{Oi}} (\gamma_{Oii-1} + \gamma_{Oii+1}) & j = i-1+n \quad i = n \\ -1 & j = i \quad n+1 \leq i \leq 2n \\ \tau_{i-ni-n} & j = i-n \quad n+1 \leq i \leq 2n \\ \tau_{i-ni-1-n} & j = i-1 \quad n+2 \leq i \leq 2n \\ \tau_{i-ni+1-n} & j = i+1 \quad n+1 \leq i \leq 2n-1 \\ 0 & \text{otherwise} \quad 1 \leq i \leq 2n \end{cases}, \quad (47)$$

and

$$b_i = \begin{cases} r_i & 1 \leq i \leq n \\ 0 & n+1 \leq i \leq 2n. \end{cases} \quad (48)$$

Eqs. 45 through 48 yield the following matrix-vector equation:

$$\mathbf{A} \vec{a} = \vec{b}. \quad (49)$$

In Eq. 49, $\mathbf{A} \in \mathbb{R}^{2n \times 2n}$ is the coefficient matrix given by

$$\mathbf{A} = [a_{ij}]_{2n \times 2n} = \begin{bmatrix} a_{1,1} & \cdots & a_{1,2n} \\ \vdots & \ddots & \vdots \\ a_{2n,1} & \cdots & a_{2n,2n} \end{bmatrix}, \quad (50)$$

with a_{ij} defined by Eq. 47, $\vec{b} \in \mathbb{R}^{2n}$ is the right-hand-side column vector given by

$$\vec{b} = [b_i]_{2n} = [b_1, \dots, b_{2n}], \quad (51)$$

with b_i defined by Eq. 48, and $\vec{p} \in \mathbb{R}^{2n}$ is the solution row vector given by

$$\vec{p} = [p_j]_{2n} = [p_1, \dots, p_2], \quad (52)$$

with p_j defined by Eq. 46.

The solution defined above can be used for constant-rate, constant-pressure, variable-rate, and variable-pressure conditions. We will explain handling production conditions after we discuss the effect of fracture flow-choking skin below.

Flow-Choking Skin. The trilinear-flow model assumes 1D linear flow within HFs; that is, it ignores the additional pressure drop, Δp_{cFi} , in each fracture of Well i due to radial convergence (choking) of flow toward the well-fracture intersection (**Fig. 5**). To incorporate the effect of radial flow convergence, we define the following flow-choking skin, s_{cFi} , as suggested by Mukherjee and Economides (1991):

$$s_{cFi} = \frac{\psi_1 k_R h}{q_R B \mu} \Delta p_{cFi} = \frac{q_i D h_D}{n_{Fi} C_{FiD} k_{fiD} x_{FiD}} \left[\ln \left(\frac{h_D}{2r_{wiD}} \right) - \frac{\pi}{2} \right]. \quad (53)$$

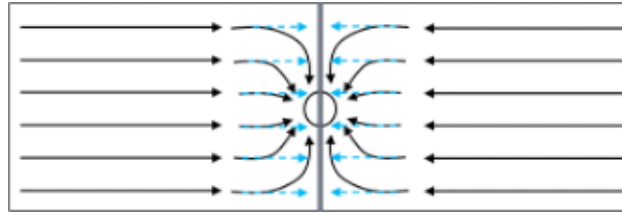


Fig. 5—Demonstration of radial flow convergence in fracture causing flow-choking skin.

Adding the choking skin, s_{cFi} , to the solution requires modifying r_i given by Eq. 36 as follows:

$$r_i = \left[\frac{\pi}{n_{Fi} C_{FiD} k_{fiD} x_{FiD} \sqrt{\alpha_{Fi}} \tanh(\sqrt{\alpha_{Fi}} x_{FiD})} + s_{cFi} \right] \bar{q}_{iD}. \quad (54)$$

Incorporation of the choking skin as described above provides a good approximation for dimensionless wellbore pressures after the end of the radial flow in HFs, which should occur earlier than the practical times of interest.

Rate-Constrained Production. For all wells starting production at the same time but at different constant rates, q_i , the \bar{q}_{iD} term in Eq. 36 is given by

$$\bar{q}_{iD} = \frac{q_{iD}}{s}. \quad (55)$$

If the wells start producing at different times, t_{i0} , and undergo a schedule of K_i rate changes, including shut-ins, then the \bar{q}_{iD} term in Eq. 36 is given by

$$\bar{q}_{iD}(s) = \frac{1}{s} \sum_{k=1}^{K_i} (q_{ikD} - q_{ik-1D}) e^{-st_{ik-1D}}. \quad (56)$$

Because the solution is in the Laplace transform domain, the results are numerically inverted into the time domain. The choice of the numerical inversion algorithm is at the discretion of the user; however, care must be taken in handling the discontinuities represented by the $e^{-st_{i-1D}}$ terms in Eq. 56. In this paper, we used the Stehfest (1970) algorithm due to its convenience and familiarity. To handle the discontinuities, we followed the suggestions of Chen and Raghavan (1996).

Wellbore Storage Effect. For the rate-constrained production conditions, the effect of wellbore storage can be incorporated into the solution by substituting \bar{p}_{wiD} obtained from the solution of Eq. 49 into the following expression (Van Everdingen and Hurst 1949):

$$\bar{p}_{wiD, \text{storage and skin}} = \frac{\bar{p}_{wiD}}{1 + C_{iD} r_{wiD}^2 s^2 \bar{p}_{wiD}}. \quad (57)$$

Incorporation of Eq. 57 into the computational algorithm is straightforward, but the numerical inversion of the multirate results with wellbore storage from the Laplace domain may be tedious.

Pressure-Constrained Production. Let $p_{wiD}(t_D)$ denote the bottomhole pressure and $q_{iD}(t_D)$ be the corresponding production rate of Well i . Let $p_{wiD,mwu}(t_D)$ represent the bottomhole pressure of Well i for $q_{iD}(t_D) = 1$; that is, $\bar{p}_{wiD,mwu}$ is the solution of Eq. 49 for unit dimensionless rate, $\bar{q}_{iD} = 1/s$. By convolution in the Laplace domain, we have the following relationship:

$$\bar{q}_{iD} = \frac{\bar{p}_{wiD}}{s \bar{p}_{wiD,mwu}}. \quad (58)$$

If each well starts producing at time $t_D = t_{0iD}$ at a specified wellbore pressure, $p_{wiD}(t_D)$, then Eq. 58 becomes

$$\bar{q}_{iD} e^{-st_{0iD}} = \frac{\bar{p}_{wiD} - \bar{p}_{wiD,s} (1 - e^{-st_{0iD}})}{s \bar{p}_{wiD,mwu}}, \quad (59)$$

where $p_{wiD,s} = p_{wiD}(t_{0iD})$ represents the shut-in pressure at the bottom of the hole at $t_D = t_{0iD}$ (due to the production of the neighboring wells, $p_{wiD,s}$ is not necessarily zero). If the wells produce at constant pressure p_{wiD} after $t_D = t_{0iD}$, then \bar{p}_{wiD} in Eqs. 58 and 59 is replaced by

$$\bar{p}_{wiD} = \frac{p_{wiD}}{s}. \quad (60)$$

Computing flow rates from Eqs. 58 or 59 requires the Laplace transform of measured bottomhole pressures (p_{wf} vs. t). There are different approaches to obtain the Laplace transform of tabulated functions (Le Page 1961; Onur and Reynolds 1998). In this work, we followed the approach suggested by Onur and Reynolds (1998).

Verification of the Model

Here, we use the existing analytical and numerical models to verify the semi-analytical model developed in this work. For analytical verification, we use the single-well trilinear model (Brown et al. 2011) and for numerical verification of multiwell results, we use a commercial software (CMG IMEX 2021).

Verification by an Analytical, Single-Well Model. For the analytical verification of the model, we have used the single-well, trilinear-flow model (Brown et al. 2011), which has the same physical assumptions. It is straightforward to show analytically that, by setting $n = 1$ and adjusting the dimensionless variables, the multiwell interference model defaults to the single-well trilinear model. Numerically, if n equally spaced, identical, horizontal wells with the same SRV and ORV properties are considered, then the pressure (or rate) responses of the wells must be the same and identical to those of a single well by the trilinear model. **Fig. 6** shows the results for three identical and equally spaced horizontal wells for the input properties given in **Table 1**. Pressure and logarithmic derivative responses obtained from the multiwell model match perfectly those of the single-well trilinear model. The expected flow-regime characteristics for wellbore storage (unit-slope of pressures and derivatives at early times before 10^{-4} days), linear flow (half-slope of the intermediate-time pressures and derivatives between 5×10^{-3} and 5×10^3 days), and boundary-dominated flow (unit-slope of the late-time derivatives after 10^4 days) are evident in the results.

Reservoir Data		Inner Reservoir (SRV) Data	
Reservoir width (equal to well length), L (ft)	5,000	Matrix bulk porosity, ϕ_{mI} (fraction)	0.05
Number of wells	3	Matrix bulk permeability, k_{mI} (md)	2.0×10^{-6}
Formation thickness, h (ft)	100	Matrix total compressibility, c_{tmI} (psi $^{-1}$)	3.0×10^{-5}
Fluid viscosity, μ (cp)	0.83	Matrix shape factor, σ_I (ft 2)	0.5
Formation volume factor, B (bbl/STB)	1.2	Natural fracture bulk porosity, ϕ_{fI} (fraction)	0.1
Well Data		Natural fracture bulk permeability, k_{fI} (md)	2.0×10^{-2}
Horizontal well length, L_h (ft)	5,000	Natural fracture total compressibility, c_{tfI} (psi $^{-1}$)	3.0×10^{-3}
Horizontal well spacing (ft)	600	Outer Reservoir (ORV) Data	
Production rate, q (STB/D)	4,000	Outer reservoir width, $2x_{eO_i}$, for $i = 1$ and 4 (ft)	100
Wellbore radius, r_w (ft)	0.3	Outer reservoir width, $2x_{eO_i}$, for $i = 2$ and 3 (ft)	200
Number of HFs, n_F	25	Matrix bulk porosity, ϕ_{mO} (fraction)	0.05
HF half-length, x_F (ft)	200	Matrix bulk permeability, k_{mO} (md)	2.0×10^{-6}
HF conductivity, k_{FWF} (md-ft)	50,000	Matrix total compressibility, c_{tmO} (psi $^{-1}$)	3.0×10^{-5}
HF aperture (width), w_F (ft)	0.1	Matrix shape factor, σ_O (ft $^{-2}$)	0.5
HF porosity, ϕ_F (fraction)	0.4	Natural fracture bulk porosity, ϕ_{fO} (fraction)	0.08
HF total compressibility, c_{tF} (psi $^{-1}$)	3.0×10^{-4}	Natural fracture bulk permeability, k_{fO} (md)	2.0×10^{-4}
Wellbore storage coefficient, C (bbl/psi)	1.0	Natural fracture total compressibility, c_{tfO} (psi $^{-1}$)	3.0×10^{-4}

Table 1—Input data for model verification by the single-well trilinear flow model.

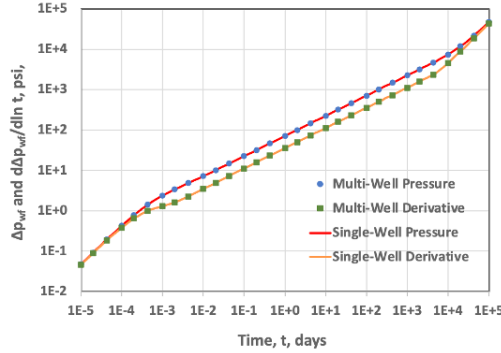


Fig. 6—Verification of the multiwell model with the analytical, trilinear, single-well model.

Verification by a Numerical Multiwell Model. For the verification of the semi-analytical model for multiwell interference, we have used the results obtained from a commercial simulator (CMG IMEX 2021). **Table 2** presents the data used for this verification, and **Fig. 7** shows a sketch and the dimensions of the multiwell system. The results are for four horizontal wells with unequal well spacing (460 ft, 500 ft, and 440 ft). Wells 1 and 3 have 25 fractures, and Wells 2 and 4 have 11 fractures.

Reservoir Data		Inner Reservoir (SRV) Data (same for all wells)	
Reservoir width, L (ft)	5,000	Matrix bulk porosity, ϕ_{mI} (fraction)	5.0×10^{-2}
Number of wells	4	Matrix bulk permeability, k_{mI} (md)	2.0×10^{-2}
Formation thickness, h (ft)	100	Matrix total compressibility, c_{tmI} (psi^{-1})	2.0×10^{-6}
Fluid viscosity, μ (cp)	0.83	Matrix shape factor, σ_I (ft^{-2})	4.8×10^{-1}
Formation volume factor, B (STB/bbl)	1.2	Natural fracture bulk porosity, ϕ_{fI} (fraction)	1.0×10^{-1}
Well Data		Natural fracture bulk permeability, k_{fI} (md)	
Horizontal well length, L_{hi} (ft)	5,000	Natural fracture total compressibility, c_{tfI} (psi^{-1})	3.0×10^{-3}
Horizontal well spacing (ft)	460, 500, 440	Outer Reservoir (ORV) Data (same for all wells except for widths)	
Production rate, q_i (STB/D)	1,000	Outer reservoir width, $2x_{eO_i}$, for $i = 1$ and 4 (ft)	10
Wellbore radius, r_{wi} (ft)	0.3	Outer reservoir width, $2x_{eO_i}$, for $i = 2, 3$, and 4 (ft)	60, 100, 40
Number of HFs on each well, n_{Fi}	25, 11, 25, 11	Matrix bulk porosity, ϕ_{mO} (fraction)	5.0×10^{-2}
HF half-length, x_{Fi} (ft)	200	Matrix bulk permeability, k_{mO} (md)	2.0×10^{-2}
HF conductivity, $k_{Fi}w_{Fi}$ (md-ft)	50,000	Matrix total compressibility, c_{tmO} (psi^{-1})	2.0×10^{-6}
HF aperture (width), w_{Fi} (ft)	0.1	Matrix shape factor, σ_O (ft^{-2})	4.8×10^{-1}
HF porosity*, ϕ_{Fi} (fraction)	0.4	Natural fracture bulk porosity, ϕ_{fO} (fraction)	1.0×10^{-1}
HF total compressibility*, c_{tFi} (psi^{-1})	3.0×10^{-4}	Natural fracture bulk permeability, k_{fO} (md)	2.0×10^{-1}
Wellbore storage coefficient, C_i (bbl/psi)	0.0	Natural fracture total compressibility, c_{tfO} (psi^{-1})	3.0×10^{-3}

*Not specified in CMG

Table 2—Input data for the verification of the multiwell model by numerical simulator.

Fig. 8 shows wellbore pressure drops computed by the analytical (this work) and numerical (CMG IMEX 2021) models. The agreement between the analytical and numerical results is excellent at late times (after ~ 500 days), but the numerical results are lower than the analytical results at earlier times. The analytical results display the expected linear-flow behavior (half-slope on log-log coordinates) at early times (less than ~ 500 days) while the log-log slope of the numerical Δp vs. time data shown in **Fig. 8** is higher than 0.5. We found that the numerical results could be improved by using smaller grids and timesteps in the simulations. However, the computational time required to generate the numerical results in **Fig. 8** was in the order of hours, and matching the early-time analytical results would require simulation times in the order of days. The computations from the analytical model, on the other hand, is instantaneous to human perception. This example does not only verify the analytical model but also highlights its importance for PTA/RTA and sensitivity studies.

Example Applications

Here, we present some examples to demonstrate important model features and its application to a field case.

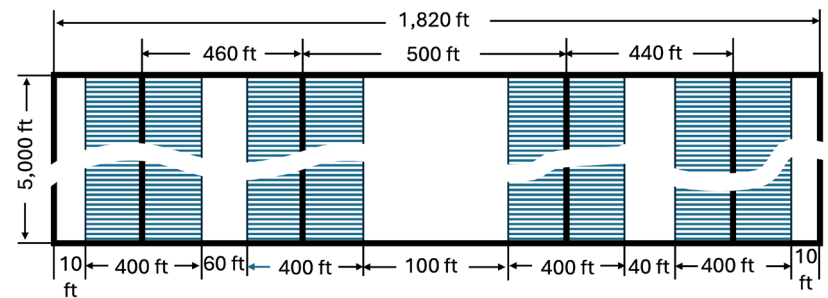


Fig. 7—Sketch of the multiwell system for the numerical verification example (drawing is not to the scale).

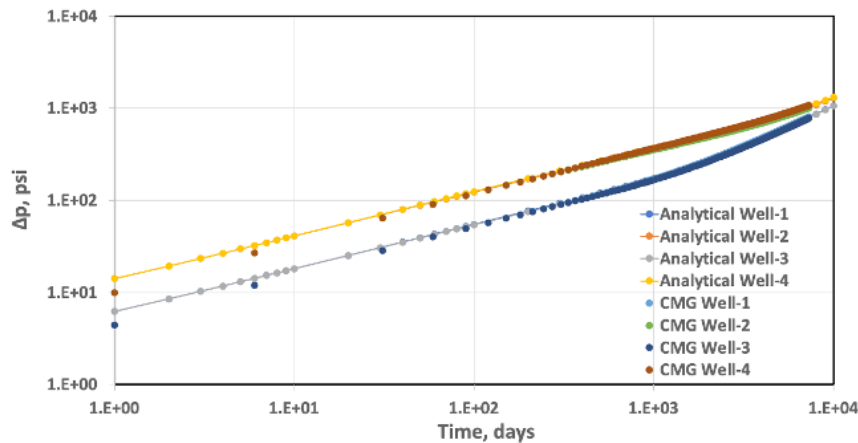


Fig. 8—Comparison of the results of the analytical (this work) and numerical (CMG IMEX 2021) models.

Example 1—Rate Variations Including Shut-In. To demonstrate the results of the model for different production schedules of wells, including shut-in periods, we consider the data in **Table 1** for three identical horizontal wells with equal well spacing. To highlight the effect of rate variations on pressure behavior, we turn off the wellbore storage effect ($C_i = 0.0 \text{ bbl/psi}$), and instead of a constant and equal flow rate for all wells, we use the production schedule shown in **Table 3**. The wells start producing at different times and follow different rate schedules. Well 3 has a shut-in period between Days 5 and 9.

Well 1		Well 2		Well 3	
Time (days)	Rate (STB/D)	Time (days)	Rate (STB/D)	Time (days)	Rate (STB/D)
0.0	0.00	0.0	0.00	0.0	0.00
1.0	1,000.00	1.0	1,000.00	3.0	1,000.00
5.0	500.00	8.0	1,500.00	5.0	0.00
10.0	2,000.00			9.0	2,500.00
				20.0	1,000.00

Table 3—Production schedules of wells for the variable-rate example (Example 1).

The results of the model for this example are shown in **Fig. 9**. Pressure behaviors in **Fig. 9** are consistent with the expectations from the rate changes of the wells. The interference of neighboring wells may not be evident in the pressure responses because they should be noticeable at later times than those considered here. We will demonstrate the effect of well interference in the next example.

Example 2—Pressure Interference of Infill (Child) Well. To highlight the effect of pressure interference between wells, we consider the data in **Table 4**. First, we let all wells start production at the same time and keep producing at the same constant rate (8,000 STB/D) at all times. Because the reservoir has uniform properties, the pressure responses of all three wells must be the same. This case is shown by the blue line in **Fig. 10**. Next, we consider the case where Well 2 is turned off. This causes a decrease in pressure drops in Wells 1 and 3 at late times (starting with a 1% decrease at ~380 days and increasing to 10% at ~2,000 days). At 10^4 days (~27 years), the decrease in the pressure drawdown of Wells 1 and 3 due to the inactivity of Well 2 is 2,260 psi (~26%). The model also provides the pressure drawdown at the location of the shut-in well (Well 2), which is shown by the green line in **Fig. 10** to reach 2,260 psi at 10^4 days.

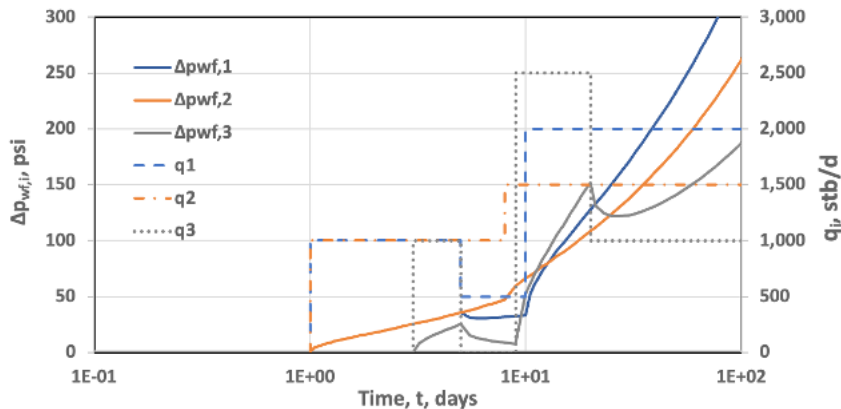


Fig. 9—Pressure behaviors of three wells for different production schedules, including a shut-in period in Well 3 (Example 1).

Reservoir Data		Inner Reservoir (SRV) Data (identical for all wells)	
Reservoir width (equal to horizontal well length), L (ft)	5,000	Matrix bulk porosity, ϕ_{mI} (fraction)	0.05
Number of wells	3	Matrix bulk permeability, k_{mI} (md)	2.0×10^{-2}
Formation thickness, h (ft)	100	Matrix total compressibility, c_{tmI} (psi^{-1})	3.0×10^{-5}
Fluid viscosity, μ (cp)	0.83	Matrix shape factor, σ_I (ft^{-2})	0.5
Formation volume factor, B (STB/bbl)	1.2	Natural fracture bulk porosity, ϕ_{fI} (fraction)	0.1
Well Data (identical for all wells)		Natural fracture bulk permeability, k_{fI} (md)	2.0×10^{-1}
Horizontal well length, L_{hi} (ft)	5,000	Natural fracture total compressibility, c_{tfI} (psi^{-1})	3.0×10^{-3}
Horizontal well spacing (ft)	300	Outer Reservoir (ORV) Data (identical for all wells)	
Production rate of active wells, q_i (STB/D)	8,000	Outer reservoir width, $2x_{eO_i}$, for $i = 1$ and 4 (ft)	50
Wellbore radius, r_{wi} (ft)	0.3	Outer reservoir width, $2x_{eO_i}$, for $i = 2$ and 3 (ft)	100
Number of HFs, n_{Fi}	25	Matrix bulk porosity, ϕ_{mO} (fraction)	0.05
HF half-length, x_{Fi} (ft)	200	Matrix bulk permeability, k_{mO} (md)	2.0×10^{-2}
HF conductivity, $k_{Fi}w_{Fi}$ (md-ft)	50,000	Matrix total compressibility, c_{tmO} (psi^{-1})	3.0×10^{-5}
HF aperture (width), w_{Fi} (ft)	0.1	Matrix shape factor, σ_O (ft^{-2})	0.5
HF porosity, ϕ_{Fi} (fraction)	0.4	Natural fracture bulk porosity, ϕ_{fO} (fraction)	0.1
HF total compressibility, c_{tFO} (psi^{-1})	3.0×10^{-4}	Natural fracture bulk permeability, k_{fO} (md)	2.0×10^{-1}
Wellbore storage coefficient, C_i (bbl/psi)	0.0	Natural fracture total compressibility, c_{tfO} (psi^{-1})	3.0×10^{-3}

Table 4—Data used in the pressure-interference example (Example 2).

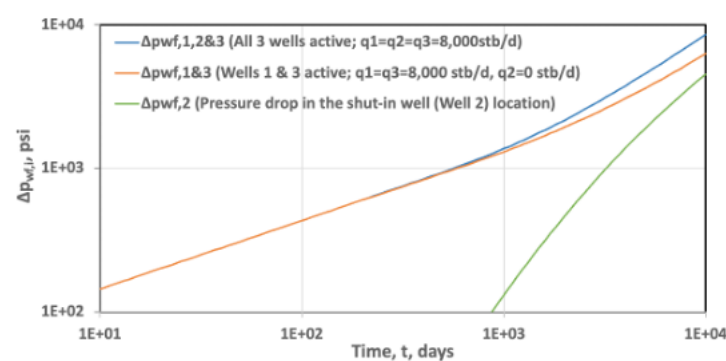


Fig. 10—Demonstration of pressure interference between neighboring wells (Example 2).

Because the logarithmic scale of **Fig. 10** visibly suppresses the magnitude of pressure interference, in **Fig. 11**, we plot the interference effect of infill Well 2 on the pressures of Wells 1 and 3. The pressure interference of the infill well (Well 2) is not practically notable on the pressure responses of Wells 1 and 3 for up to a year (magnitudes less than 8 psi by the 370th day of uninterrupted production). At the 5th year (1,825 days), the magnitude of pressure interference is ~ 200 psi (**Fig. 11**), and at the 10th year (3,650 days), it reaches ~ 615 psi. It must be noted that the magnitude of interference at a given time will depend on the properties of the ORVs between wells. For this example, we exaggerated the conductivities of the ORVs (making them close to the properties of the SRVs) to highlight the interference effect. For tighter ORVs, the interference effect may be visible even later (beyond the economic production lives of the wells).

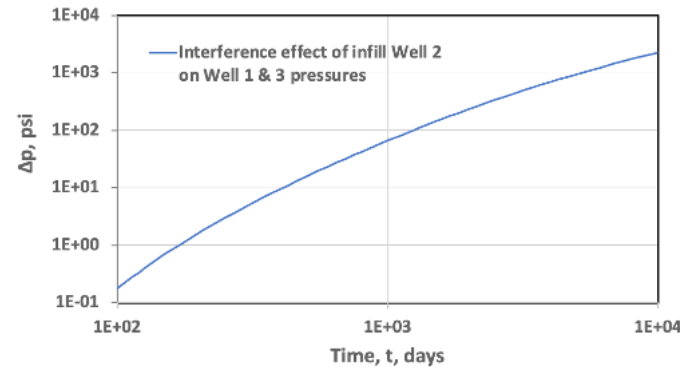


Fig. 11—Magnitude of interference of Well 2 on Well 1 and Well 3 pressures (Example 2).

Example 3—Production Interference of Infill (Child) Well. This example demonstrates the interference of an infill (child) well with the production behavior of two existing (parent) wells. For the purposes of this discussion, wells are assumed to have the same SRV and ORV properties. However, they have different HF stages and properties. The parent wells are 1,640 ft apart and start producing at the same time. The infill (child) well is drilled 180 days (4,320 hours) after the existing (parent) wells at a distance of 1,000 ft from Parent Well 1 and 640 ft from Parent Well 2. All three wells are assumed to produce at a constant bottomhole pressure drop of 3,000 psi with respect to the initial reservoir pressure. Pertinent data for this example are presented in **Table 5**.

Well spacing (ft)			
Parent Well 1 to Parent Well 2 = 1,640 ft; Parent Well 1 to Infill Well = 1,000 ft			
Well Properties			
Parent or infill well	Parent Well 1	Parent Well 2	Infill Well
Production starting times, t_0 (hours)	0	0	4,320
Bottomhole pressure drop (constant), Δp_{wf} (psi)	3,000	3,000	3,000
Well length, L_h (ft)	5,000	5,000	5,000
Wellbore radius, r_w (ft)	0.3	0.3	0.3
Number of HFs, n_F	13	25	25
HF half-length, x_F (ft)	660	300	300
HF conductivity, k_{FWF} (md-ft)	10,000	5,000	5,000
HF width, w (ft)	0.1	0.1	0.1
HF porosity, ϕ_F (fraction)	0.4	0.4	0.4
HF total compressibility, c_{tF} (psi $^{-1}$)	3.00×10^{-5}	3.00×10^{-5}	3.00×10^{-5}
Common Properties			
Viscosity, μ (cp)		0.8	
Formation volume factor, B (STB/bbl)		1.1	
Formation thickness, h (ft)		80	
Outer Reservoir			
Matrix permeability, k_{mO} (md)		3.59×10^{-5}	
Matrix porosity, ϕ_{mO} (fraction)		0.05	
Matrix total compressibility, c_{tmO} (psi $^{-1}$)		2.00×10^{-5}	
Shape factor, σ_O (ft $^{-2}$)		0.009	

Table 5—Data used in the production-interference example (Example 3).

Well spacing (ft)	Parent Well 1 to Parent Well 2 = 1,640 ft; Parent Well 1 to Infill Well = 1,000 ft
Fracture permeability, k_{fO} (md)	0.1
Fracture porosity, ϕ_{fO} (fraction)	0.0001
Fracture compressibility, c_{fO} (psi^{-1})	1.00×10^{-4}
Outer reservoir width, $2 x_e$ (ft)	40
Inner Reservoir	
Matrix permeability, k_{mI} (md)	3.59×10^{-5}
Matrix porosity, ϕ_{mI} (fraction)	0.05
Matrix total compressibility, c_{tmI} (psi^{-1})	3.00×10^{-5}
Shape factor, σ_I (ft^{-2})	0.009
Fracture permeability, k_f (md)	1
Fracture porosity, ϕ_f (fraction)	0.001
Fracture total compressibility, c_{tf} (psi^{-1})	1.70×10^{-4}

Table 5 (continued)—Data used in the production-interference example (Example 3).

Fig. 12 shows the production rates of the parent and child wells for the scenario considered in this example. The effect of the child well's production is immediately noticeable on the production rates of the parent wells at 4,320 hours. It is important to note that this is different from the gradual manifestation of the infill well's influence on the pressure responses of parent wells in Example 2 because the production rate is not only a function of the flowing bottomhole pressure but also the average pressure in the well's drainage area, which is increased when the child well starts producing (due to the reduction of each well's drainage area).

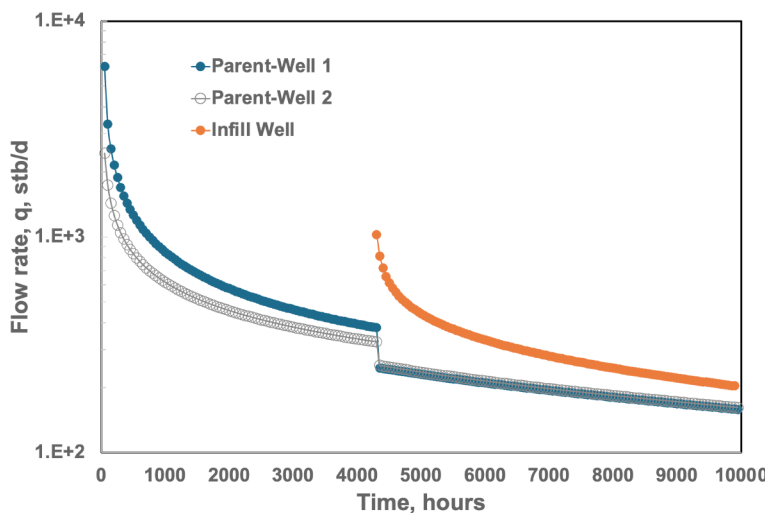


Fig. 12—Production-rate interference of a child well on parent wells (Example 3).

The drop in the production rates of the parent wells because of the production of the child well is not an indication of the drop in productivity of the individual wells or the overall system. As noted above, the decrease in the drainage area of each well increases their respective average pressures, $p_{avg,i}$, and the productivity of each well $[q_i / (p_{avg,i} - p_{wf,i})]$ increases. Consequently, the total productivity of the multiwell system increases as the number of wells increases, though at a decreasing rate, as the drainage area of each well decreases.

For the example considered here, **Fig. 13** shows that although the cumulative productions of the parent wells decrease due to the influence of the child well, the cumulative production of the total (three-well) system increases. The increase in the system's cumulative production due to the 236.7 days of production of the child well is ~10% [370,040 bbl without the child well and 407,070 bbl with the child well at 10,000 hours (416.7 days)]. If this increase in the cumulative production of the system justifies drilling the infill well, interference does not have negative consequences. However, interference due to the so-called “frac-hits” deserves a different discussion, which will be covered in the “Discussion” section below.

Example 4—Rate Interference of Child Wells. In **Fig. 14**, we demonstrate the interference effect of child wells on rate-transient behavior. We consider a parent well and two child wells starting production at 4,020 hours and 6,020 hours after the parent well. All three wells produce at a constant bottomhole pressure (the bottomhole pressure of the parent well is reduced by an additional 1,000 psi concurrent with the start of the production of Child Well 1). The properties of the reservoir (SRVs and ORVs) are the same as those in **Table 5** (Example 3). The spacing and properties of the wells in this example are given in **Table 6**.

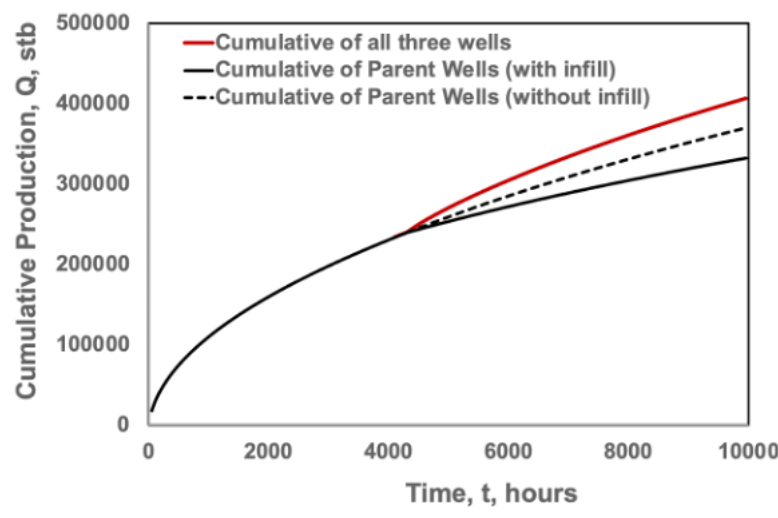


Fig. 13—Change in cumulative production due to an infill well (Example 3).

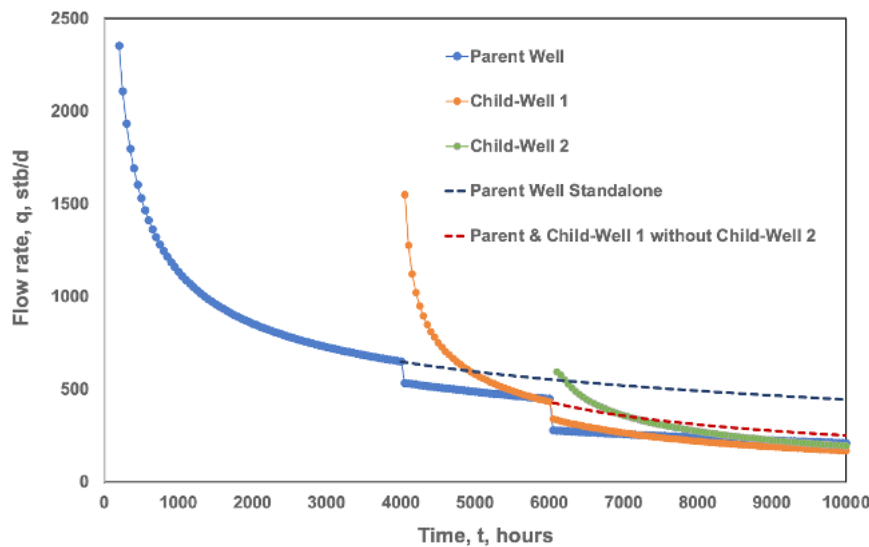


Fig. 14—Rate-transient trends due to interference of child wells (Example 4).

Well spacing (ft)	Parent well to child well = 1,000 ft; Child Well 1 to Child Well 2 = 640 ft		
Well Properties	Parent well	Child Well 1	Child Well 2
Parent or infill well			
Production starting times, t_0 (hours)	0	4,020	6,020
Bottomhole pressure drop (constant), Δp_{wf} (psi)	3,000 psi until 4,020 hours; 4,000 psi after 4,020 hours	2,000	2,000
Well length, L_h (ft)	5,000	5,000	5,000
Wellbore radius, r_w (ft)	0.3	0.3	0.3
Number of HFs, n_F	13	25	25
HF half-length, x_F (ft)	660	300	300
HF conductivity, k_{FWF} (md-ft)	10,000	5,000	5,000
HF width, w (ft)	0.1	0.1	0.1
HF porosity, ϕ_F (fraction)	0.4	0.4	0.4
HF total compressibility, c_{IF} (psi^{-1})	3.00×10^{-5}	3.00×10^{-5}	3.00×10^{-5}

Table 6—Well data for rate-transient effect of child wells (Example 3).

As expected, **Fig. 14** shows that drilling a new well introduces new transients and causes a drop in the production rates of the existing wells. This is consistent with the expectations and field observations. In the next example, we will use this feature of the model to analyze a field example.

Example 5—Field Example. This interference example is from the Eagle Ford Formation. The data were presented by Kurtoglu and Salman (2015) and also analyzed by Chu et al. (2020a). The details of the field case have been discussed by Kurtoglu and Salman (2015) and Chu et al. (2020b) and will not be repeated here. **Table 7** provides a summary of the case data. For the information not specified in the literature, we have either made assumptions or obtained the data from the model match. It is important to note that the child well is longer (6,900 ft) than the parent well (5,000 ft). Because our model assumes equal well lengths, we had to make an adjustment. Considering that the driving parameter of the model is the HF spacing, we used the given fracture spacing as an initial guess and adjusted the number of fractures on a 5,000-ft child well based on the match of the rate responses (highlighted in bold in **Table 7**).

	Our Model		Literature Data	
	Parent	Child	Parent	Child
Bottomhole pressure drops (constant), Δp_{wf} (psi)	3,000 psi until child, 4,000 psi thereafter	1,000	Constant bottomhole pressure, not specified	
Well lengths, L_h (ft)	5,000	5,000	5,000	6,900
Number of HFs, n_F	13	25	13	35
Wellbore radius, r_w (ft)		0.3	Not specified	
Viscosity, μ (cp)		0.8	Not specified	
Formation volume factor, B (STB/bbl)		1.1	Not specified	
Formation thickness, h (ft)		80	Not specified	
Outer Reservoir				
Matrix permeability, k_{mO} (md)		3.59×10^{-5}		3.59×10^{-5}
Matrix porosity, ϕ_{mO} (fraction)		0.05		0.05
Matrix total compressibility, c_{tmO} (psi^{-1})		2.00×10^{-5}	Not specified	
Shape factor, σ_O (ft^2)		0.009	Not specified	
Fracture permeability, k_{fO} (md)		0.1	1 md for SRV	
Fracture porosity, ϕ_{fO} (fraction)		0.0001	Not specified	
Fracture compressibility, c_{tfO} (psi^{-1})		1.00×10^{-4}	Not specified	
Outer reservoir width, $2 x_e$ (ft)		40		40
Inner Reservoir				
Matrix permeability, k_{mI} (md)		3.59×10^{-5}		3.59×10^{-5}
Matrix porosity, ϕ_{mI} (fraction)		0.05		0.05
Matrix total compressibility, c_{tmI} (psi^{-1})		3.00×10^{-5}	Not specified, but $\omega = 0.1$	
Shape factor, σ_I (ft^2)		0.009	Not specified, but $\lambda = 3.00 \times 10^{-8}$	
Fracture permeability, k_{fI} (md)		1		1
Fracture porosity, ϕ_{fI} (fraction)		0.001	Not specified, but $\omega = 0.1$	
Fracture total compressibility, c_{tfI} (psi^{-1})		1.70×10^{-4}	Not specified, but $\omega = 0.1$	
HFs				
HF half-length, x_F (ft)	660	300	660	300
HF conductivity, k_{FWF} (md-ft)	10,000	5,000	10,000	5,000
HF width, w_F (ft)		0.1	Not specified	
HF porosity, ϕ_F (fraction)		0.4	Not specified	
HF total compressibility, c_{tF} (psi^{-1})		3.00×10^{-5}	Not specified	

Table 7—Properties used to match the Eagle Ford example data (Example 5).

Fig. 15 shows the match of the field data with our model (with the properties in the “Our Model” column of **Table 7**). The match is acceptable within the uncertainties of the data and the inherent nonuniqueness of the inverse solution process. **Fig. 16** compares the

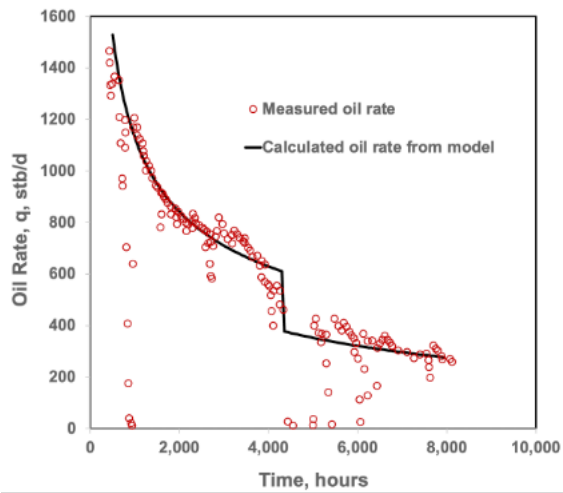


Fig. 15—Matching measured production rate vs. time with the results of the model developed in this work (Example 5).

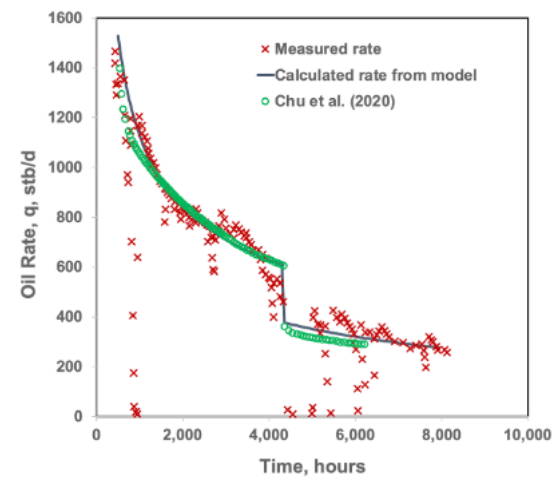


Fig. 16—Comparison of the matches with the measured data by our model and that of Chu et al. (2020a) (Example 5).

matches obtained with our model and by Chu et al. (2020a). Arguably, our match looks slightly more successful, but given the uncertainties in the data and differences in modeling assumptions, the decision lies within the knowledge and experience of the analyst. [Chu et al. (2020a) model can incorporate unequal horizontal well lengths but assumes uniform reservoir properties, whereas our model assumes equal well lengths but can incorporate the stimulation effects within SRVs.]

Example 6—Effect of Well Completion and Stimulation. To demonstrate the use of the model to examine the effect of different well-completion and -stimulation scenarios, we consider the three-well case in Example 2, but we treat Well 2 as an infill well candidate. For the base case, we assume the infill well (Well 2) is completed with the same design and stimulation treatment as Wells 1 and 2 (three identical wells) and use the data in **Table 4**. Because the design and SRV properties of the wells are the same, their pressure behaviors are the same as shown by the blue line in **Fig. 17**.

Next, we consider doubling the number of fracture stages (from 25 to 50) on Well 2 and assume that this treatment will improve the properties of its SRV as shown in **Table 8**. (The new stimulation is assumed to increase not only the matrix and fracture permeability and compressibility in the SRV but also the dual-porosity shape factor, σ_{12} , due to the finer cracking of the SRV matrix.) The corresponding pressure behavior of Well 2 is shown by the orange line in **Fig. 17**. There is a considerable improvement in the productivity of Well 2 (lower pressure drawdown at the same rate) because of the new completion design and stimulation treatment. The performance improvement in Well 2 is in the form of accelerated production. The early-time pressure drawdown of Well 2 is significantly lower than that for the original design initially and increases faster at late times. **Fig. 17** does not show any change in the pressure behaviors of Wells 1 and 3 due to the change in the stimulation treatment of Well 2. As discussed in Example 2, any such effect should become noticeable at later times.

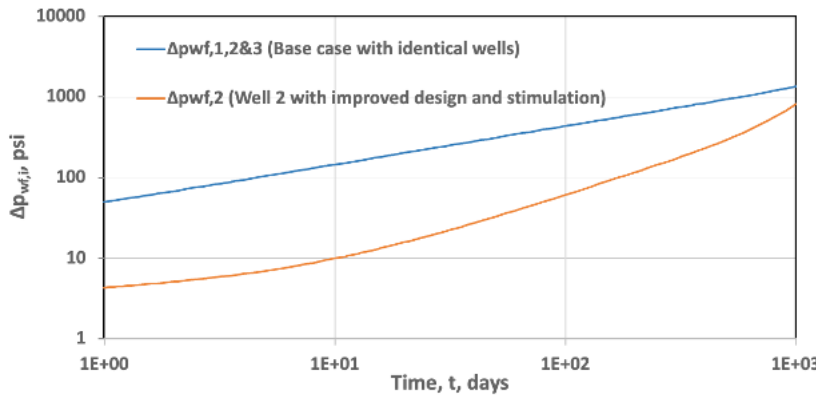


Fig. 17—Effect of improved well design and stimulation treatment (Example 6).

Matrix bulk porosity, ϕ_{mI} (fraction)	0.05
Matrix bulk permeability, k_{mI} (md)	2.0
Matrix total compressibility, c_{tmI} (psi $^{-1}$)	3.0×10^{-3}
Matrix shape factor, σ_I (ft $^{-2}$)	2.0
Natural fracture bulk porosity, ϕ_fI (fraction)	0.1
Natural fracture bulk permeability, k_fI (md)	20.0
Natural fracture total compressibility, c_{tfI} (psi $^{-1}$)	3.0×10^{-3}

Table 8—Assumed inner reservoir (SRV) properties of Well 2 after new stimulation treatment with 50 fractures (Example 6).

Discussion

Some comments about the difference of our model from the existing models are in order. These comments should also shed light on the nature of parent- and child-well interactions. In the “Introduction” section, we mentioned that the models by Molina (2019), Chu et al. (2020a), and Hamdi et al. (2021) may bear some relevance (and resemblance) to ours. As also noted in the introduction, the usefulness of analytical models depends on their simplicity and computational speed compared to more elaborate numerical models. This is achieved by simplifying assumptions in the development of analytical models without compromising key physical flow features.

Chu et al. (2020b) used the conventional method of superposition to develop an analytical multifracture, multiwell solution from single-fracture solutions. However, this approach required uniform properties in the entire reservoir and could not consider the differences between stimulated and unstimulated reservoirs around wells. Another simplifying assumption used by Hamdi et al. (2021) is the communicating-tanks representation of reservoir blocks with different properties. This approach is akin to coarse-grid numerical simulation, where pressure transients in the reservoir blocks are approximated by a succession of pseudosteady states. The applicability of this approximation depends on the validity of the pseudosteady-flow assumption in the blocks. Because the higher the permeability, the earlier the pseudosteady state, the success of the Hamdi et al. (2021) model requires smaller block sizes (fine grid) and smaller timesteps as the permeability decreases. Therefore, for a tight matrix of unconventional reservoirs, the accuracy required for PTA and RTA applications can be achieved at high computational costs.

The approach used by Molina (2019) is closer to our model development and deserves more scrutiny. Molina (2019) extends the trilinear-flow model suggested by Brown et al. (2011) for a single horizontal well to multiple wells in unconventional reservoirs. This is the same idea we used in our model development. The trilinear-flow approach is suitable if the well and reservoir configurations justify the linear-flow assumption in the SRVs, ORVs, and HFs. We appreciate the rigor of Molina’s mathematical development, but we disagree with his assumptions based on our perceptions of reality. First, we are not keen on the extension of our original trilinear-flow concept (Brown et al. 2011) to quadruple or higher linear-flow elements because it is an overstretch of the mutually-linear-flow assumption in the SRV and ORV. If multiple blocks are needed to represent flow in the SRV and ORV of the well, this implies multidimensional flow convergence in the system. Then one needs to give up the convenience of linear-flow assumption and use a boundary-element method (e.g., Medeiros et al. 2010). For the same reason, we disagree with the extension of the model to unequal well lengths and frac-hits because they cause nonlinear flow convergences.

Second, the representation of frac-hits as cross-cutting fractures having their own SRVs is not consistent with the physical reality. Frac-hits are caused by runaway fractures in the presence of cross-cutting, weakness planes (local stress heterogeneities). In these cases, fractures may grow along the weakness plane instead of creating a complex fracture network (SRV) away from the fracture face, which is against the desired fracture-stimulation effect for unconventional (for the fracture length to increase, fluid leakoff from the fracture face must be limited). As shown by Gaol (2015), cross-cutting, standalone fractures do not create a considerable impact on the pressure and production responses of the wells they connect. What is represented in Molina’s model (Molina 2019) are locally overlapping SRVs of the wells, which also defies the linear-flow assumption (in the case of a mildly nonuniform SRV, a single, rectangular SRV may be a more suitable approximation).

Most importantly, Molina (2019) assumes a fixed no-flow boundary between wells and determines its position based on the proportion of the fracture half-lengths of the wells. In principle, the location of the no-flow boundary between wells depends on their production rates

(drainage areas of wells in a multiwell system are proportional to their production rates), and if the production rates are not constant, their drainage boundaries will be moving. As discussed in Examples 3 and 4 above, when the no-flow boundary moves between wells, the change in the drainage areas (shrinkage or expansion), and the resulting change in average pressures also change the productivity of the wells. Therefore, the fixed no-flow-boundary assumption of Molina (2019) renders his model unsuitable for the analysis of dynamic interference effects.

Final Remarks

The analytical model presented in this paper is robust and versatile for practical problems with multiple wells in unconventional reservoirs. As with any model, however, its success is constrained by its assumptions. Moreover, the model is not intended to be an all-inclusive and high-precision solution. Generally, it is as accurate as the trilinear-flow assumption, which has found some useful applications since its introduction (Brown et al. 2011). The model and the computational algorithm should be useful for PTA and RTA applications, production-data analysis, performance predictions, and as a tool to make decisions on well spacing, well design, and HF stimulation treatments. In this work, several synthetic, forward-modeling examples have been presented to verify the model, demonstrate its versatility, and provide test cases for potential developers. The field example demonstrates the versatility and success of the model for applications to real data.

The model has been presented for single-phase oil flow. Its extension to single-phase gas flow by pseudopressure transformation (Al-Hussainy et al. 1966) is straightforward. Extensions to multiphase flow are more involved but also possible using suitable multiphase pseudopressure transformations (e.g., Jones and Raghavan 1988; Poe 2014). Similarly, pseudopressure transformation may be used to include pressure-dependent properties in the model (e.g., Wang et al. 2022).

Nomenclature

B	formation volume factor, STB/bbl
c_t	total compressibility, psi ⁻¹
C_i	wellbore storage constant, bbl/psi
C_D	wellbore storage coefficient, dimensionless
C_{FD}	HF conductivity, dimensionless
C_{RD}	reservoir conductivity, dimensionless
f	dual-porosity transfer function, dimensionless
G	Green's function, dimensionless
h	formation thickness, ft
k	permeability, md
L	horizontal well length, ft
n_F	number of HFs on a horizontal well, dimensionless
p	pressure, psi
q	production rate, STB/D
r_w	wellbore radius, ft
s	Laplace transform parameter, dimensionless
s_{cF}	fracture choking skin, dimensionless
t	time, days
v	volumetric flow velocity, ft/D
x	x -coordinate or distance, ft
x_{eo}	outer reservoir half-width, ft
x_F	HF half-length, ft
y	y -coordinate or distance, ft
y_e	half-distance between two hydraulic fractures, ft
z	z -coordinate or distance, ft
Δp	pressure drop from initial pressure, psi
η	diffusivity constant, md·psi/cp
λ	transmissibility ratio, dimensionless
μ	viscosity, cp
σ	matrix shape factor, ft ⁻²
ϕ	porosity, fraction
ω	storativity ratio, dimensionless

Subscripts

avg	= average
D	= dimensionless
e	= external
f	= fracture
F	= hydraulic fracture
HF	= hydraulic fracture
i	= well index
ini	= initial
I	= inner reservoir
K	= reservoir block type, I , O , or, HF
m	= matrix
O	= outer reservoir
R	= reference

References

- Acuna, J. A. 2023. Application of Fractional Dimension RTA to Gas Wells in Haynesville Including Parent-Child Effects. Paper presented at the SPE/AAPG/SEG Unconventional Resources Technology Conference, Denver, Colorado, USA, 13–15 June. <https://doi.org/10.15530/urtec-2023-3852016>.
- Ajani, A. and Kelkar, M. 2012. Interference Study in Shale Plays. Paper presented at the SPE Hydraulic Fracturing Technology Conference, The Woodlands, Texas, USA, 6–8 February. <https://doi.org/10.2118/151045-MS>.
- Al-Hussainy, R., Ramey, H. J., and Crawford, P. B. 1966. The Flow of Real Gases Through Porous Media. *J Pet Technol* **18** (5): 624–636. <https://doi.org/10.2118/1243-A-PA>.
- Brown, M. ., Ozkan, E. ., Raghavan, R. . et al. 2011. Practical Solutions for Pressure-Transient Responses of Fractured Horizontal Wells in Unconventional Shale Reservoirs. *SPE Res Eval & Eng* **14** (6): 663–676. <https://doi.org/10.2118/125043-PA>.
- Chen, C.-C. and Raghavan, R. 1996. An Approach to Handle Discontinuities by the Stehfest Algorithm. *SPE J.* **1** (4): 363–368. <https://doi.org/10.2118/28419-PA>.
- Chu, H., Liao, X., Chen, Z. et al. 2020a. Rate-Transient Analysis of a Constant-Bottomhole-Pressure Multihorizontal Well Pad with a Semianalytical Single-Phase Method. *SPE J.* **25** (6): 3280–3299. <https://doi.org/10.2118/203842-PA>.
- Chu, W.-C.-C., Pandya, N. D., Flumerfelt, R. W. et al. 2019. Rate-Transient Analysis Based on the Power-Law Behavior for Permian Wells. *SPE Res Eval & Eng* **22** (4): 1360–1370. <https://doi.org/10.2118/187180-PA>.
- Chu, W.-C., Scott, K. D., Flumerfelt, R. et al. 2020b. A New Technique for Quantifying Pressure Interference in Fractured Horizontal Shale Wells. *SPE Res Eval & Eng* **23** (1): 143–157. <https://doi.org/10.2118/191407-PA>.
- CMG IMEX. 2021. *Black-Oil and Unconventional Simulator*. Calgary, Alberta, Canada: Computer Modelling Group Ltd. <https://www.cmg.ca/solutions/software/imex/>.
- de Swaan, O. A. 1976. Analytic Solutions for Determining Naturally Fractured Reservoir Properties by Well Testing. *SPE J.* **16** (3): 117–122. <https://doi.org/10.2118/5346-PA>.
- Gao, A. M. L. 2015. *Interference Test Analysis with Two Fractured Horizontal Wells*. MSc thesis, Colorado School of Mines, Golden, Colorado, USA.
- Hamdi, H., Behmanesh, H., and Clarkson, C. R. 2021. A Simple Method for Quantifying Inter-Well Communication Using Production Data from Single-Phase Shale Gas Reservoirs. Paper presented at the SPE Annual Technical Conference and Exhibition, Dubai, UAE, 21–23 September. <https://doi.org/10.2118/205839-MS>.
- Jones, J. R. and Raghavan, R. 1988. Interpretation of Flowing Well Response in Gas-Condensate Wells. *SPE Form Eval* **3** (3): 578–594. <https://doi.org/10.2118/14204-PA>.
- Kazemi, H. 1969. Pressure Transient Analysis of Naturally Fractured Reservoirs with Uniform Fracture Distribution. *SPE J.* **9** (4): 451–462. <https://doi.org/10.2118/2156-A>.
- Kurtoglu, B. and Salman, A. 2015. How to Utilize Hydraulic Fracture Interference to Improve Unconventional Development. Paper presented at the Abu Dhabi International Petroleum Exhibition and Conference, Abu Dhabi, UAE, 9–12 November. <https://doi.org/10.2118/177953-MS>.
- Le Page, W. R. 1961. *Complex Variables and the Laplace Transform for Engineers*. New York, USA: Dower Publications Inc.
- Lerza, A., Mamani, M., Puidengolas, M. et al. 2022. Well Completion Performance Analysis in the Vaca Muerta Formation by Leveraging Fractional Dimension RTA - Case of Study. Paper presented at the SPE/AAPG/SEG Unconventional Resources Technology Conference, Houston, Texas, USA, 20–22 June. <https://doi.org/10.15530/urtec-2022-3726020>.
- Medeiros, F., Ozkan, E., and Kazemi, H. 2010. A Semianalytical Approach To Model Pressure Transients in Heterogeneous Reservoirs. *SPE Res Eval & Eng* **13** (2): 341–358. <https://doi.org/10.2118/102834-PA>.
- Molina, O. M. 2019. Analytical Model to Estimate the Fraction of Frac Hits in Multi-Well Pads. Paper presented at the SPE/AAPG/SEG Unconventional Resources Technology Conference, Denver, Colorado, USA, 22–24 July. <https://doi.org/10.15530/urtec-2019-238>.
- Mukherjee, H. and Economides, M. J. 1991. A Parametric Comparison of Horizontal and Vertical Well Performance. *SPE Form Eval* **6** (2): 209–216. <https://doi.org/10.2118/18303-PA>.
- Onur, M. and Reynolds, A. C. 1998. Numerical Laplace Transformation of Sampled Data for Well-Test Analysis. *SPE Res Eval & Eng* **1** (3): 268–277. <https://doi.org/10.2118/36554-PA>.
- Poe, B. D. 2014. Production Performance Evaluation of Wells Completed in Unconventional Reservoirs Using Capillary Pressure Data and Relative Permeability Effects. Paper presented at the SPE Annual Technical Conference and Exhibition, Amsterdam, The Netherlands, 27–29 October. <https://doi.org/10.2118/170940-MS>.
- Stehfest, H. 1970. Algorithm 368: Numerical Inversion of Laplace Transforms [D5]. *Commun ACM* **13** (1): 47–49. <https://doi.org/10.1145/361953.361969>.
- Van Everdingen, A. F. and Hurst, W. 1949. The Application of the Laplace Transformation to Flow Problems in Reservoirs. *J Pet Technol* **1** (12): 305–324. <https://doi.org/10.2118/949305-G>.
- Wang, G., Zhang, R., and Cui, L. 2022. Transient Pressure Behavior of a Horizontal Well in a Naturally Fractured Gas Reservoir with Dual-Permeability Flow and Stress Sensitivity Effect. *Geofluids* **2022**: 1–11. <https://doi.org/10.1155/2022/5993701>.

Appendix A—Problem Formulation for the Outer and Inner Reservoirs and HFs

Here we explain, briefly, the problem formulation for the outer and inner reservoirs and HFs and present the solution for each region. Details of the HF solutions are provided in Appendix B.

Outer Reservoirs. The formulation and solution of the problems for Outer Reservoirs 1 and $n + 1$ are similar because they include one no-flow boundary and one boundary in contact with an SRV (**Fig. A-1**, top images). Problems for Outer Reservoirs 2 through n are the same (**Fig. A-1**, bottom image).

Outer Reservoir O_i for $i = 1$ and $n + 1$. Outer Reservoir O_1 has one no-flow boundary at $x_{O1} = x_{Oe1}$ and another boundary in contact with $I1$ (Inner Reservoir 1) at $x_{O1} = -x_{Oe1}$ (**Fig. A-1**, top left image). The diffusivity equation for the fracture system of $O1$ is given (in the Laplace domain) by

$$\frac{d^2 \bar{p}_{fO1D}}{dx_{O1D}^2} - u_{O1} \bar{p}_{fO1D} = 0. \quad (\text{A-1})$$

The external boundary of $O1$ at x_{eO1} is assumed to be a no-flow boundary (a drainage boundary between two parallel horizontal wells or an impermeable physical boundary) given by

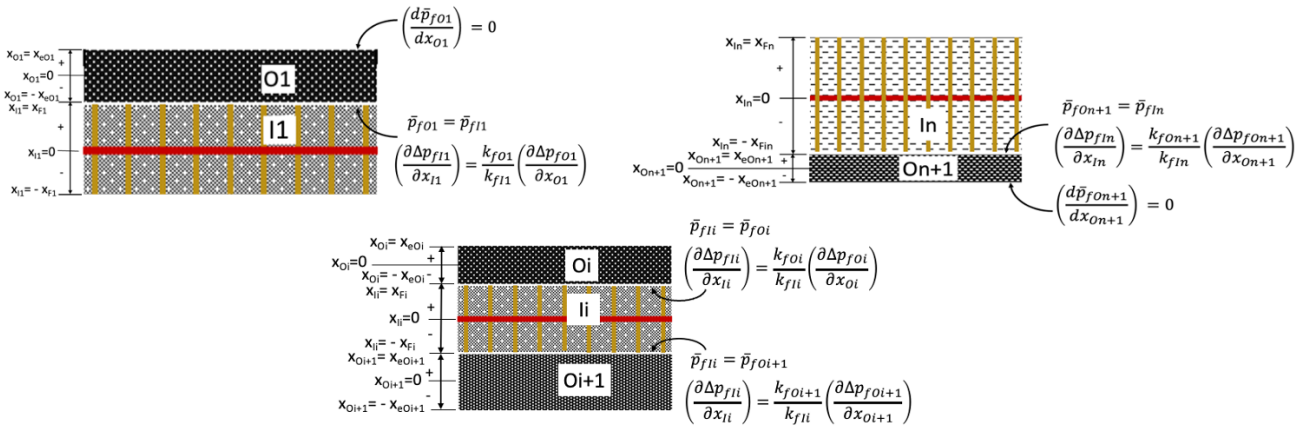


Fig. A-1—Geometry, notations, and boundary conditions for the O1 (top left), On+1 (top right), and Oi (bottom) problems.

$$\left(\frac{d\bar{p}_{f01D}}{dx_{O1D}} \right)_{x_{O1D}=x_{eO1D}} = 0. \quad (\text{A-2})$$

At the inner boundary of \$O1\$ (\$x_{O1} = -x_{eO1}\$), the pressures of \$I1\$ and \$O1\$ must be equal; that is,

$$\bar{p}_{f01D}(-x_{eO1D}) = \bar{p}_{f1D}(x_{F1D}). \quad (\text{A-3})$$

The solution of the boundary value problem for \$O1\$ (Eqs.A-1 through A-3) is straightforward and given (in terms of the dimensionless pressure of \$I1\$, \$\bar{p}_{f1D}\$) by

$$\bar{p}_{f01D}(x_{O1D}) = \left(\bar{p}_{f1D} \right)_{x_{F1D}} \frac{\cosh[\sqrt{u_{O1}}(x_{O1D} - x_{eO1D})]}{\cosh(2\sqrt{u_{O1}}x_{eO1D})}. \quad (\text{A-4})$$

Outer reservoir \$On+1\$ is the mirror image (flipped vertically) of \$O1\$ (Fig. A-1, right image); it has the no flow boundary at \$x_{On+1} = -x_{eOn+1}\$ and the boundary in contact with \$In\$ at \$x_{On+1} = x_{eOn+1}\$. The solution of the boundary value problem for \$On+1\$ follows the same lines as in \$O1\$ and yields

$$\bar{p}_{f0n+1D}(x_{On+1D}) = \bar{p}_{fInD}(x_{FnD}) \frac{\cosh[\sqrt{u_{On+1}}(x_{On+1D} + x_{eOn+1D})]}{\cosh(2\sqrt{u_{On+1}}x_{eOn+1D})}. \quad (\text{A-5})$$

Outer Reservoir \$Oi\$ for \$2 \leq i \leq n\$. Outer Reservoir \$Oi\$, \$2 \leq i \leq n\$, has one boundary in contact with \$Ii-1\$ at \$x_{Oi} = x_{eOi}\$ and another boundary in contact with \$Ii\$ at \$x_{Oi} = -x_{eOi}\$ (Fig. A-1, bottom image). The diffusivity equation for the fracture system of \$Oi\$ is the same as that for \$O1\$ or \$On+1\$, with the subscripts replaced by the index \$i\$ for \$2 \leq i \leq n\$. The boundary conditions at \$x_{Oi} = x_{eOi}\$ and \$x_{Oi} = -x_{eOi}\$ meet the requirement of pressure continuity with \$Ii-1\$ and \$Ii\$ given, respectively, by

$$\bar{p}_{f0iD}(x_{eOiD}) = \bar{p}_{fli-1D}(-x_{F_{i-1}D}) = \bar{p}_{fli-1D}(x_{F_{i-1}D}) = \bar{p}_{f0i-1D}(-x_{eO_{i-1}D}), \quad (\text{A-6})$$

and

$$\bar{p}_{f0iD}(-x_{eOiD}) = \bar{p}_{fliD}(x_{F_{iD}}) = \bar{p}_{fliD}(-x_{F_{iD}}) = \bar{p}_{f0i+1D}(x_{eO_{i+1}D}). \quad (\text{A-7})$$

The solution of the boundary value problem for \$Oi\$ for \$2 \leq i \leq n\$ is given by

$$\begin{aligned} \bar{p}_{f0iD}(x_{OiD}) &= \bar{p}_{fli-1D}(x_{F_{i-1}D}) \left\{ e^{\sqrt{u_{Oi}}(x_{OiD} - x_{eOiD})} + e^{-2\sqrt{u_{Oi}}(x_{eOiD})} \frac{\sinh[\sqrt{u_{Oi}}(x_{OiD} - x_{eOiD})]}{\sinh[2\sqrt{u_{Oi}}(x_{eOiD})]} \right\} \\ &\quad - \bar{p}_{fliD}(x_{F_{iD}}) \frac{\sinh[\sqrt{u_{Oi}}(x_{OiD} - x_{eOiD})]}{\sinh[2\sqrt{u_{Oi}}(x_{eOiD})]}. \end{aligned} \quad (\text{A-8})$$

Inner Reservoirs. As shown in Fig. A-2, Inner Reservoirs \$I1\$ (top left image) and \$In\$ (top right image) are the mirror images of each other (flipped vertically). Inner Reservoir \$I1\$ has mutual boundaries with Outer Reservoirs \$O1\$ and \$O2\$ and Inner Reservoir \$In\$ has common boundaries with Outer Reservoirs \$On\$ and \$On+1\$. Inner Reservoirs \$Ii\$, \$2 \leq i \leq n-1\$ (bottom image in Fig. A-2), are contiguous to Outer Reservoirs \$Oi\$ and \$O_{i+1}\$ as shown in Fig. A-2 (bottom image).

The diffusion equations for all Inner Reservoirs \$Ii\$, \$1 \leq i \leq n\$, can be written in the following general form:

$$\frac{d^2 \bar{p}_{fliD}}{dy_{liD}^2} - \alpha_{Oi} \bar{p}_{fliD} + \bar{h}_i = 0, \quad (\text{A-9})$$

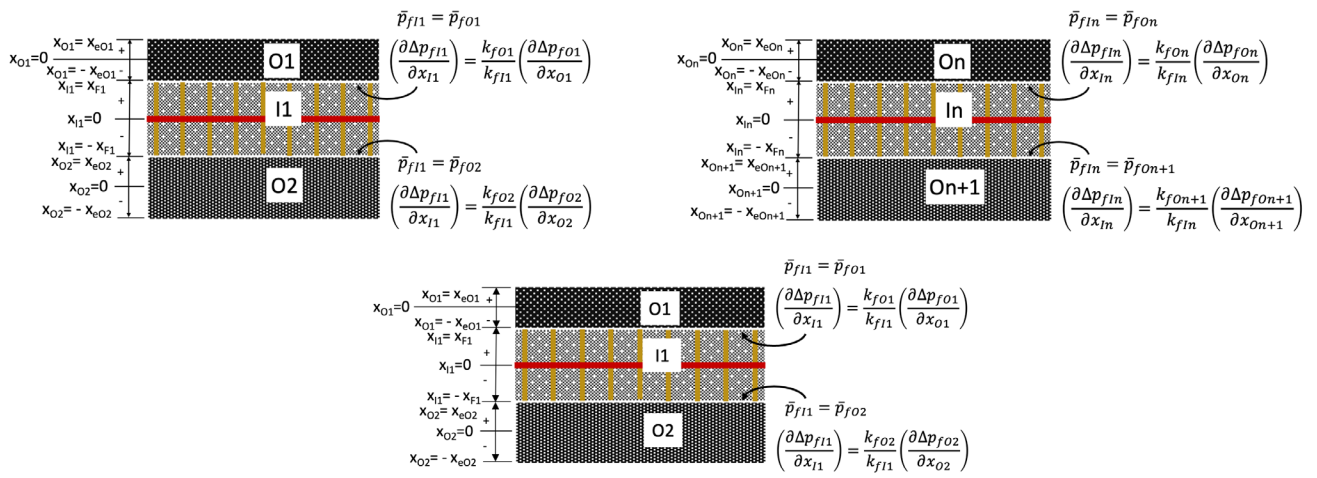


Fig. A-2—Geometry, notations, and boundary conditions for *I1* (left), *In* (right), and *II* (bottom) problems.

where α_{O_i} and \bar{h}_i are defined by Eqs. 41 and 35, respectively, in the text. We have pressure continuity at $y_{liD} = 0$ expressed by

$$\bar{p}_{fiD}(y_{liD} = 0) = \bar{p}_{FiD}, \quad (\text{A-10})$$

and a no-flow boundary at $y_{liD} = 1$ expressed by

$$\left(\frac{d\bar{p}_{fiD}}{dy_{liD}} \right)_{y_{liD}=1,s} = 0. \quad (\text{A-11})$$

Structurally, the diffusion equation in Eq. A-9 is different from those for the outer reservoirs because of the existence of the forcing function, \bar{h}_i , which represents the pressure interference of the neighboring wells. The interferences of the neighboring wells enter the solution in terms of their average pressures, $\bar{p}_{fiD,\text{avg}}$, in the y_{liD} -direction along the SRV boundary of Well i . This is by the 1D (in x -direction) flow assumption in the outer reservoirs, which implies that the outer reservoirs average out the pressures along the SRV boundaries of the adjoining inner reservoirs. The expressions for $\bar{p}_{fiD,\text{avg}}$ are obtained in Appendix B. The solution to the inner reservoir problems is given by

$$\bar{p}_{fiD}(y_{liD}, s) = \frac{\cosh[\sqrt{\alpha_{O_i}}(1-y_{liD})]}{\cosh(\sqrt{\alpha_{O_i}})} \bar{p}_{fiD}(0, s) + \frac{\bar{h}_i}{\alpha_{O_i}} \left\{ 1 - \frac{\cosh[\sqrt{\alpha_{O_i}}(1-y_{liD})]}{\cosh(\sqrt{\alpha_{O_i}})} \right\}, \quad (\text{A-12})$$

where, by the continuity of pressure, $\bar{p}_{fiD}(0, s) = \bar{p}_{FiD}(s)$.

Hydraulic Fractures. Below, we first explain the inner boundary condition for HF and then present the formulation and solution of the HF problem.

Fracture Inner Boundary Condition. The inner boundary of the HF is the cylindrical intersection surface ($2\pi r_w w_{Fi}$) with the horizontal well (Fig. A-3). However, by the 1D, linear-flow assumption in the fracture (in the x_{HFi} -direction), the wellbore surface is represented

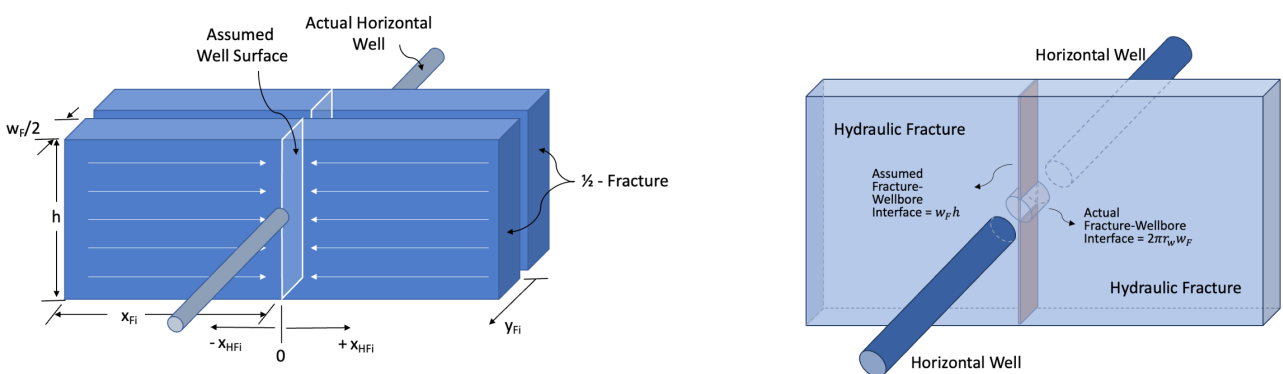


Fig. A-3—Fracture geometry and the assumed well surface due to 1D flow.

by a rectangular plane at $x_{HF_i} = 0$ with the width, w_{Fi} , and height, h , of the fracture. (The radial convergence of the flow lines around the well-fracture intersection is incorporated into the solution through a flow-choking skin defined by Eq. 53 in the text.)

Assuming linear flow in HFs (in the x_{HF_i} -direction), the velocity of fluid crossing the vertical plane at $x_{HF_i} = 0$ is

$$v_{x_{HF_i}} = -\frac{\psi_1 k_{Fi}}{2\pi\mu} \left(\frac{\partial \Delta p_{Fi}}{\partial x_{HF_i}} \right)_{x_{HF_i}=0}. \quad (\text{A-13})$$

Fluxes passing through the plane at $x_{HF_i} = 0$ in the positive and negative x_{HF_i} -directions are identical due to symmetry. (This symmetry is a result of the trilinear-flow assumption, which implies that the influxes from the outer reservoirs at $x_{li} = x_{Fi}$ and $x_{li} = -x_{Fi}$ are instantaneously and homogeneously distributed in the x_{li} -direction in the inner reservoir so that the flow in the inner reservoir remains to be predominantly 1D in the y_{li} direction.) We model $\frac{1}{2}$ of the fracture width ($w_{Fi}/2$) in the positive y_{Fi} -direction as the (repetitive) symmetry element (Fig. A-3), which produces $\frac{1}{2}$ of the fracture flow rate. Therefore, the flow rate, q_{Fi} , passing through both sides of the rectangular plane at $x_{HF_i} = 0$ is given by

$$q_{Fi} = 2v_{x_{HF_i}} w_{Fi} h = -\frac{\psi_1 k_{Fi} w_{Fi} h}{\pi\mu} \left(\frac{\partial \Delta p_{Fi}}{\partial x_{HF_i}} \right)_{x_{HF_i}=0}. \quad (\text{A-14})$$

Because we assume n_{Fi} identical fractures uniformly spaced along the horizontal well, the individual fracture flow rate, q_{Fi} , in Eq. A-14 is related to the horizontal well flow rate q_i by

$$q_{Fi} = \frac{q_i B}{n_{Fi}}. \quad (\text{A-15})$$

Substituting Eq. A-15 into Eq. A-14, converting to dimensionless variables, and taking the Laplace transform yields

$$\left(\frac{d\bar{p}_{FiD}}{dx_{HFiD}} \right)_{x_{HFiD}=0} = -\frac{\pi \bar{q}_{iD}}{n_{Fi} C_{FiD} k_{liD} x_{FiD}}. \quad (\text{A-16})$$

Hydraulic Fracture, HF, Problem. Flow from Inner Reservoir li to Hydraulic Fracture HF_i is assumed to be linear in the y_{Fi} -direction, and flow from the HF to the wellbore is also assumed to be linear in the x_{HFi} -direction. Fluid entering the HF from the inner reservoir at $y_{Fi} = w_{Fi}/2$ is instantaneously and uniformly distributed across the half-width ($w_{Fi}/2$) of the fracture and $\partial \Delta p_{Fi} / \partial x_{HFi}$ and $\partial \Delta p_{Fi} / \partial t$ are independent of y_{Fi} . Also considering that $y_{Fi} = 0$ is the line of symmetry and, thus, a no-flow boundary, the dimensionless diffusivity equation for the HF is given (in Laplace domain) by

$$\frac{d^2 \bar{p}_{FiD}}{dx_{HFiD}^2} + \frac{2}{w_{FiD}} \left(\frac{d\bar{p}_{FiD}}{dy_{FiD}} \right)_{y_{FiD}=w_{FiD}/2} - \frac{s}{\eta_{FiD}} \bar{p}_{FiD} = 0. \quad (\text{A-17})$$

We consider the continuity of fluxes of the inner reservoir and fracture at the face of the fracture ($y_{FiD} = w_{FiD}/2$) as follows:

$$\left(\frac{d\bar{p}_{FiD}}{dy_{FiD}} \right)_{y_{FiD}=w_{FiD}/2} = \frac{w_{FiD}}{C_{FiD} \tilde{v}_{liD} x_{FiD}} \left(\frac{d\bar{p}_{liD}}{dy_{liD}} \right)_{y_{liD}=0}. \quad (\text{A-18})$$

From Eq. A-12, we have

$$\left(\frac{d\bar{p}_{liD}}{dy_{liD}} \right)_{y_{liD}=0} = -\beta_{Fi} \bar{p}_{liD}(s) + \frac{\beta_{Fi}}{\alpha_{Oi}} \bar{h}_i, \quad (\text{A-19})$$

where β_{Fi} and \bar{h}_i are given by Eqs. 35 and 39, respectively, in the text, and we have substituted $\bar{p}_{liD}(0, s) = \bar{p}_{liD}(s)$.

Using Eqs. A-18 and A-19, we can write the diffusion equation for HFs (Eq. A-17) as follows:

$$\frac{d^2 \bar{p}_{FiD}}{dx_{HFiD}^2} - \alpha_{Fi} \bar{p}_{FiD} + \frac{\gamma_{Fi}}{\alpha_{Oi}} \bar{h}_i = 0, \quad (\text{A-20})$$

where γ_{Fi} and α_{Fi} are defined in the text by Eqs. 37 and 38, respectively.

The boundary conditions of the fracture problem are no flow across the tip of the fracture (at $x_{HFiD} = x_{FiD}$), given by,

$$\left(\frac{d\bar{p}_{FiD}}{dx_{HFiD}} \right)_{x_{HFiD}=x_{FiD}} = 0, \quad (\text{A-21})$$

and prescribed flux at the horizontal well intersection ($x_{HFiD} = 0$) given by Eq. A-16. The solution of Eq. A-20 subject to the conditions in Eqs. A-21 and A-16 is given by

$$\bar{p}_{FiD}(x_{HFiD}, s) = \frac{\gamma_{Fi}}{\alpha_{Fi} \alpha_{Oi}} \bar{h}_i + \frac{\pi \bar{q}_{iD} \cosh [\sqrt{\alpha_{Fi}} (x_{FiD} - x_{HFiD})]}{n_{Fi} C_{FiD} k_{liD} x_{FiD} \sqrt{\alpha_{Fi}} \sinh (\sqrt{\alpha_{Fi}} x_{FiD})}. \quad (\text{A-22})$$

Because of the pressure continuity at the interface between the HFs and wellbores, the dimensionless wellbore pressures are readily written from Eq. A-22 as follows:

$$\bar{p}_{wiD}(s) = \bar{p}_{FiD}(x_{HFID} = 0, s) - \frac{\gamma_{Fi}}{\alpha_{Fi}\alpha_{O_i}}\bar{h}_i = r_i; \quad 1 \leq i \leq n, \quad (\text{A-23})$$

where

$$r_i = \frac{\pi \bar{q}_{iD}}{n_{Fi} C_{FiD} k_{JiD} x_{FiD} \sqrt{\alpha_{Fi}} \tanh(\sqrt{\alpha_{Fi}} x_{FiD})}, \quad (\text{A-24})$$

and \bar{h}_i is given by Eq. 35 in the text.

Appendix B—Average Inner Reservoir Pressures

In the inner reservoir solution (Eq. A-12) and wellbore pressure solution (Eq. A-23) include $\bar{p}_{JiD,\text{avg}}$ (through the \bar{h}_i terms, Eq. 40 in the text) as an approximation to $\bar{p}_{JiD}(y_{iD})$. Here $\bar{p}_{JiD,\text{avg}}$ is the average of $\bar{p}_{JiD}(y_{iD})$ in the y_{iD} -direction along the SRV boundary of Well i ; that is,

$$\bar{p}_{JiD,\text{avg}} = \int_0^1 \bar{p}_{JiD}(y_{iD}, s) dy_{iD}; \quad i = 1, \dots, n. \quad (\text{B-1})$$

Substituting Eq. A-12 into Eq. B-1, we obtain

$$\bar{p}_{JiD,\text{avg}} = \varepsilon_i \bar{p}_{FiD} + (\varepsilon_i - 1) \frac{1}{\alpha_{O_i}} (1 - \varepsilon_i) \bar{h}_i(s); \quad i = 1, \dots, n, \quad (\text{B-2})$$

where we have defined

$$\varepsilon_i = \frac{\tanh(\sqrt{\alpha_{O_i}})}{\sqrt{\alpha_{O_i}}}; \quad i = 1, \dots, n. \quad (\text{B-3})$$

If we define

$$\tau_{ij} = \begin{cases} \varepsilon_i & j = i, \quad 1 \leq i \leq n \\ (1 - \varepsilon_1) \frac{\gamma_{O12}}{\alpha_{O1}} & j = 2, \quad i = 1 \\ (1 - \varepsilon_n) \frac{\gamma_{Onn-1}}{\alpha_{On}} & j = n - 1, \quad i = n \\ (1 - \varepsilon_i) \frac{\gamma_{Oij}}{\alpha_{O_i}} & \text{otherwise,} \end{cases} \quad (\text{B-4})$$

we can write Eq. B-2 as follows:

$$\bar{p}_{JiD,\text{avg}} = \begin{cases} \tau_{11} \bar{p}_{FI1D} + \tau_{12} \bar{p}_{FI2D,\text{avg}} & i = 1 \\ \tau_{ii} \bar{p}_{FIiD} + \tau_{i-1} \bar{p}_{Ji-1D,\text{avg}} + \tau_{i+1} \bar{p}_{Ji+1D,\text{avg}} & 2 \leq i \leq n - 1 \\ \tau_{nn} \bar{p}_{FIuD} + \tau_{n-1} \bar{p}_{Ji-1D,\text{avg}} & i = n. \end{cases} \quad (\text{B-5})$$